Escola de Camins
Escola Tècnica Superior d'Enginyeria de Camins, Canals i Ports
UPC BARCELONATECH

TREBALL FINAL DE MÀSTER

Damage and modelling of composite materials for the automotive industry.

Treball realitzat per:
Ana Salas Ordóñez

Dirigit per:
Dr. Sergio Oller Martinez
Dra. Lucia Gratiela Barbu
Eduardo Martín Santos

Master en:
Numerical Methods in Engineering

Barcelona, June 2017

Departament d'Enginyeria Civil i Ambiental

DAMAGE AND FAILURE MODELLING OF COMPOSITE MATERIALS FOR THE AUTOMOTIVE INDUSTRY

Ana Salas Ordóñez

Escola Tècnica Superior d'Enginyers de Camins, Canals i Ports de Barcelona

Universitat Politècnica de Catalunya

Master Thesis
Numerical Methods in Engineering

Advisors:
Dr. Sergio Oller Martinez
Dra. Lucia Gratiela Barbu
Eduardo Martín Santos

June 2017

Abstract

Fibre-reinforced polymer-based composite materials fail due to a wide variety of interacting damage mechanisms, which require complex constitutive models in order to develop Finite Element (FE) predictive analysis. In the design of automotive components, the whole body of the vehicle is needed to be modelled for certain simulations. This makes necessary a computationally-efficient constitutive model in order to get a proper definition of its behaviour. In this master thesis, the model published by Martín-Santos et al. in 2013 is taken as a reference, in order to take advantadge of the simplified loading functions and the reduced mesh influence in the results due to the implementation of the Crack Band Methodology.

In this work, the model is upgraded to be able to reproduce the behaviour of a wider range of materials than the original model, and to become more stable in simulations regarding extreme loading conditions, as the crushing of the composite due to an axial impact event. The proposed constitutive model is implemented in Pam-Crash FE code, in order to take advantage of its well-proved experience in explicit analysis of specimens under dynamic loads in the automotive industry.

The implementation is validated by comparing the results of FE predictions with experimental data from delamination and low-velocity impact tests. A good correlation between the numerical and experimental results is achieved when using a bilinear cohesive law, for the different models.

Acknowledgements

I would like to thank all the people that have contributed, in one way or another, to the realization of this project.

First of all, I would like express my gratitude to my advisors, Eduardo Martín, Lucia Gratiela and Sergio Oller for the opportunity of working with them, for the knowledge provided and for their dedication during these months, helping me to grow professionally and personally.

I would like to acknowledge IDIADA Automotive Technology S.A. for giving me the opportunity to develop myself professionally in their facilities and to carry out this project with them. Also, the Polytechnic University of Catalonia (UPC) and the International Center for Numerical Methods in Engineering (CIMNE) for all opportunities to attend many lectures and seminars during these two years, which have helped me to acquire the necessary knowledge to develop a project like this.

Last but not least, I want to thank my family and friends for their unconditional support. Specially to my colleagues and friends Daniel, Lisandro and Carles for their willingness to share their knowledge at any time as well as for their company.

Contents

List of Figures

List of Figures

List of Figures

List of Tables

List of Tables

Chapter 1

Introduction and objectives

1.1 Background

In material science, most of the phenomenological models predicting material behaviour are generally based on experimental observations. The main challenge is understanding and elaborating constitutive laws which predict material response for different loading scenarios. In the last century, extensive research on isotropic materials such as steel, or aluminium, has provided reliable elastic, elasto-plastic and failure models which are nowadays used routinely by engineers. However, research in composite materials is still challenged by fully understanding and reproducing the phenomena.

In the automotive framework, the manufacturing of components conformed by composite materials, specially the case of fibre-reinforced polymers (FRP), is a topic with a growing interest. It is mainly motivated by the need of weight reduction in the body of the vehicle, specially with the apparition of the electric-powered vehicle. In passenger vehicles, the ability to absorb impact energy of composite materials makes them an interesting option for the occupant safety framework. This is called the crashworthiness of the strucutre. Originally, the target was to produce very stiff, quasi-non-deformable cars. Over the years, crashworthiness strategies have evolved in order to improve the safety of the passengers, producing vehicles with highly deformable and predictable energy absorbing zones at the front and rear, and a rigid passenger safety shell in between. Composite structures offer excellent crash performances, with specific energy absorptions exceeding those of metals.

However, the use of structural composites in high volume car production is still somewhat limited due to the cost of the raw materials and the lack of suitable manufacturing processes. Composite processing times are relatively long, raw materials are relatively expensive and high quality surface finishes are difficult to achieve. Regarding the manufacturing process, tools for composite production are much cheaper than tools for sheet metal forming, since composite processes are one-shot operations, while sheet metal forming requires five-six separate tools per component line. These savings are only influential at low production volumenes while at higher volumenes part costs dominate.

Experimental testing for the development of crashworthy vehicles is very costly and it requires the use of highly specialised test facilities. For this reason, in the automotive framework crash simulation tools have been extensively developed since the beginning of the computer era. Thus, the proper characterization and definition of the constitutive behaviour of materials are required in order to simulate complete car models in different crash conditions. FRP materials were only interesting until a short time ago for the aeronautical sector, which shows different design requirements, and therefore a different research strategy, not including the analysis of simulations over dynamic events. Therefore, a major challenge relating to automotive composite design is the availability of simulation tools and a general lack of composite material characterization.

1.2 Motivation

Fibre-reinforced polymer-based composite materials fail in a combination of wide variety interacting damage machanisms, which require complex constitutive models in order to develop Finite Elements (FE) predictive analysis. While there are numerous progressive and failure models that predict mechanical response, the current failure models are not accurate for all loading configurations, boundary conditions, lay-ups and thicknesses of composite laminates.

In this framework, IDIADA leaded the SUPERCALCULUS project. This was a European project founded by the CDTI, in which the next partners were involved: IDIADA (project leader and final customer), AMADE (material testing and development of simu-

lation methodologies), AERNNOVA (manufacturing and testing) and the university Carlos III (Material testing). One of the objectives of that project was to develop a tool package for the improvement of the analysis of the mechanical properties and simulation of FRP under low-velocity impact (LVI) loading. For this, a material model in ABAQUS was developed for the simulation of fabric-reinforced composites. On the other side, ESI, which is developer of the PAM-CRASH software, was partner of the project, so numerical tools for the simulation of LVI loading were developed for both solvers.

As a conclusion of that study, ABAQUS was found to have a weak performance under explicit integration scheme where a high level of non-linearity are produced. This is specially notorious when delamination between composite plies needs to be modelated. This leads to a complex modelling methodology which is not feasible for the modelling of large components. PAM-CRASH was found to have a strong formulation for the simulation of dynamic events and in the delamination between plies, but a lack on the ply modelling, since results obtained by means of the constitutive models for the ply simulation shown to be mesh depencency. Thus, the material card properties in the ply need to be adapted if different element sizes are used. A numerical tool was developed in order to define properly the constitutive law in PAM-CRASH for different element sizes. The project resulted into a successful development of these tools focused on the automotive industry, achieving a proper correlation of large specimens, in a reasonable computational time. Currently, the methodologies developed on that project are being applied in ongoing projects for the simulation of complete car tests.

Even though a good level of correlation was achieved with the application of the models available in PAM-CRASH, in the 2016 release of the software the implementation of user sub-routines for the ply modelling is possible. Thus, with this capability, IDIADA wants to improve the numerical tools that are currently being applied for the simulation of LVI loading over specimens conformed by FRP. For this, the model developed in the SUPERCALCULUS with the University of Girona (Udg) would be taken as a reference in order to implement a new model in PAM-CRASH, updating the reference model with the improvements developed by IDIADA and its experience in this framework for the last years.

1.3 Objectives

The main objective of the thesis is the development, implementation and validation of a constitutive model for the simulation of carbon fibre reinforced polymers under impact loading in Pam-Crash FE code using Fortran. The automotive industry requirements are taken into account in order to be applicable on ongoing projects. For this effect, the following targets should be considered:

- Increase the applications and capabilities of the material model published by Idiada and the Udg in 2014.
- The implementation of this model in the Pam-Crash solver, in order to have the best combination of predictive tools for the simulation of the behavior of FRP components: The methodologies developed in Abaqus and the wide experience in the simulation of dynamic events in Pam-Crash.
- The analysis of correlation and performance of the different methodologies developed in this project, with the numerical tools previously developed in the Supercalculus.

1.4 Outline of the thesis

In this section the contents of this document are briefly presented. The document begins with a review on properties of composite materials, as well as a brief introduction of the current status of crash behaviour of composite materials in different FE softwares.

The following chapter contains a review of the state of the art on Continuum Damage Mechanics (CDM) applied to the damage analysis of fibre-reinforced composites. Then, a constutitve model based on the CDM is presented for fabric-reinforced composite plies under in-plane loads.

In chapter 4, the basic concepts regarding the finite element analysis are briefly presented, followed by the explanation of the numerical aspects to be taken into account in the implementation in Fortran of the Continuum Damage model presented in Chapter 3.

Regarding the material characterization, in chapter 5 experimental tests required to obtain the properties of the materials used in this project are briefly explained. Then, the properties of two fibre-reinforced composite materials are presented: Unidirectional carbon-reinforced composite (CC) and fabric carbon-reinforced composite (TC).

The numerical models used to validate the model implemented in Pam-Crash are presented in chapter 6. Each section corresponds to a different test: one element, delamination and low velocity impact tests. In addition, a discussion of some problems involving the change of Pam-Crash version in the models presented in Supercalculus is made.

Validation of the constitutive formulation is done in Chapter 7 by the presentation of results and discussion of the numerical tests presented in the previous chapter.

The final chapter states the conclusions and the future work lines of this master thesis.

Chapter 2

Literature review

In this chapter a literature study of relevant information concerning composite materials and their status in crash simulations is conducted. For this, basic concepts of composite materials are presented in the first section. The second section goes into more detail in the properties that characterize fibre-reinforced composites (FRPs), which are the ones studied in this project. Finally, the status of composites in crash simulation softwares is briefly presented.

2.1 Composite materials

Composite materials, referred to as composites, are conformed by a combination of two or more materials on a macroscopic scale. Conventionally one of the materials is used as a reinforcement, in a disperse phase. This material contributes to certain properties, as the stiffness, strength or fatigue life. The other material present in a composite material is usually conformed in a continuous phase, contributing to properties as the shape stability, or protecting the reinforcement for corrosion. This project is focused on fibre-reinforced polymeric materials, which are usually conformed by two phases (Figure 2.1): the continuous phase is the matrix, which is a polymer, metal or ceramic and the dispersed phase can be particles, fibres or sheets. The type and quantity of the reinforcement determine the final properties of the composite. Therefore, composite materials can be classified according to the matrix material and the reinforcement geometry.

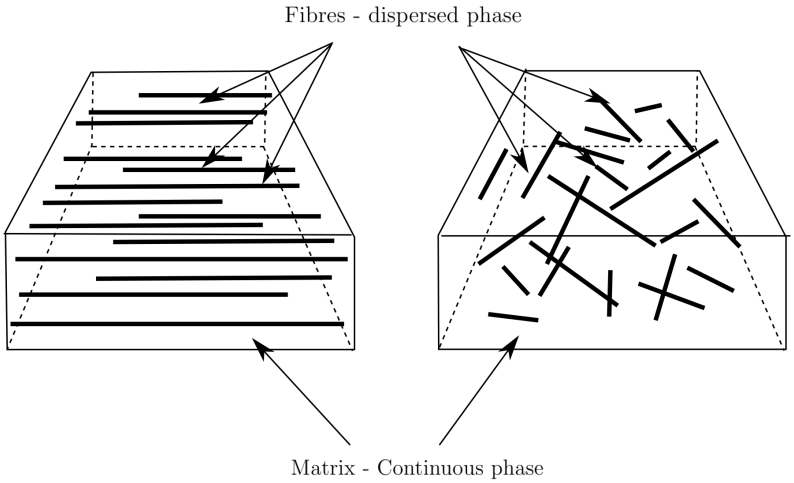

Figure 2.1: Phases of a composite material.

According to the type of reinforcement they can be classified as particle-reinforced, fibre-reinforced and structural (Figure 2.2), presenting the following properties:

Particle-reinforced composites consist of a matrix reinforced with a dispersed phase in form of particles. They can be divided into two different groups depending on the size of the particles: large-particle composites, in which the particles restrain the movement of the matrix, and dispersion-strengthened composites, in which the matrix endures the major portion of the applied load and the particles obstruct dislocation motion. This type of composites achieve gains in stiffness primarily, but also can achieve increases in strength and toughness. However, the improvements are less than what would be achieved in a fibre-reinforced composite. One extended application of this kind of composites can be found in the trims inside the vehicle (door, dashboard..) which are usually conformed by Polypropylene or a similar polymer, reinforced with talc, in order to increase the stiffness while maintaining the component thickness. The principal advantage of particle reinforced composites is their low cost and ease of production and forming. In applications showing low load requirements, these particles are sometimes used for weigh or cost reduction, instead of improving capabilities.

Fibre-reinforced composites consist of a matrix reinforced with a dispersed phase in form of fibres which improves strength, stiffness and fracture toughness of the material, difficulting crack growth in the directions normal to the fiber. The FRPs can be divided

into two different groups: short fibre reinforced polymers and long fibre polymers. The strengthening effect depends on the fibre length and its orientation with respect to the stress direction, being higher in long-fibre (continuous-fibre) reinforced composites than in short-fibre (discontinuous-fibre) reinforced composites. For continuous-fibre reinforced composites, when the fibres are aligned they provide maximum strength but only along the direction of alignment, while it gets considerable weaker along other directions and is therefore highly anisotropic. While for discontinuous-fibre reinforced composites the properties are considered isotropic.

Structural composites include the laminated materials, which stack different layers with different properties to conform the composite material. A wide range of materials can be designed under this methodology, from the stacking of fibre-reinforced layers in different orientations, to the manufacturing of a windshield in a vehicle, conformed by two layers of glass embedding one adhesive layer. Laminated composites then, can be conformed both with a single material in different orientations, or by the combination of different materials. One case of special interest in this category of materials are the sandwhich laminates, which have a central layer conformed by a foam, or another material in honeycomb-like structures. In this case, the bending stress of the laminate is increased avoiding an excessive increase on its weight and, in the case of foam-reinforced sandwiches, the acoustic behaviour is improved.

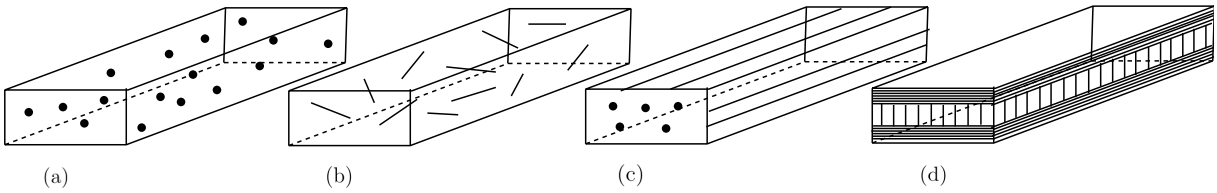

Figure 2.2: Types of reinforcement. (a) Particle-reinforced. (b) Fibre-reinforced (discontinuous-fibre). (c) Fibre-reinforced (continuous-fibre). (d) Structural Sandwich.

This thesis is however only going to be focused on laminated composites of fibre reinforced polymers (FRPs) due to its importance in the automotive industry.

2.2 Fibre-reinforced composites

As it has been explained in the previous section, a fibre-reinforced polymer is a composite material made of a polymer matrix reinforced with fibres, commonly used in the aerospace, automotive, marine and construction industries. They are widely used in the automotive industry due to the high specific stiffness and the ability to dissipate high levels of energy under impact and crashworthiness events. The fibers are usually glass, carbon, or aramid while the polymer is usually an epoxy or polyester resin. Generally, they have a brittle-elastic behaviour and a relatively poor transverse or shear resistance [5].

FRPs can be of single-layer or multi-layer type. The single-layer type includes composites conformed by one layer. Composites where different layers are stacked, but with the material orientation in the same direction are included in this group. The multi-layered composites are formed by several layers stacked with their fibres oriented in different directions. Each layer can be unidirectional, when all fibres in that specific layer are aligned in one direction, or fabric, when the fibres have two or more directions [6]. Thus, fibre-reinforced composites materials can be classified into two main categories: Unidirectional and fabric-reinforced composites (Figure 2.3).

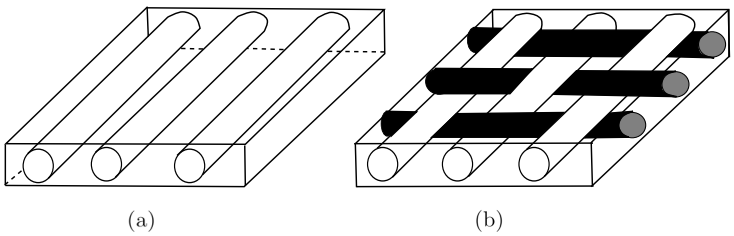

Figure 2.3: Types of fibre-reinforced composite. (a) Unidirectional. (b) Fabric-reinforced.

Due to the effect of fibre waviness, fabric-reinforced composites present lower in-plane stiffness and ultimate strength than unidirectional ply laminates. On the other hand, their tow waviness reinforce the properties throughout the thickness offering higher damage tolerance and energy absorption [4]. Moreover, this, combined with the outstanding drapeability which allows manufacturing flexibility, makes these materials a suitable option for car manufacturers in mass produced vehicles, compared with conventional metallic alloys.

2.3 Crash behaviour of composites in FEM simulations

Several commercial Finite Element (FE) codes such as LS-DYNA, Radioss and Pam-Crash have been developed specially for impact and nonlinear dynamic simulations, based on explicit time integration formulation. In the framework of crash behaviour when composite materials are involved, the different codes show different proposals for the simulation of their constitutive behaviour, based on different Continuum Damage Mechanics models.

The first meso-scale damage approach was proposed by Ladevèze [7], in which in-ply and delamination failure are modelled for unidirectional composites (UD) based on the assumption that the damage is uniform through the thickness of individual layers. On the other hand, Matzenmiller et al. developed an in-plane anisotropic model for the onset and evolution of damage at the laminate level for UD composites [13].

Ladevèze constitutive model has been adapted by other authors in order to simulate the behaviour of fabric-reinforced composites. For instance, Hochard et al. adapted the Ladeveze damage model in order to predict damage evolution and failure in textile composites [9], extending later the model to simulate the behaviour under fatigue conditions [10]. On the other hand, Johnson et al. presented a CDM model for fabric-reinforced composites based on Ladevèze model for modelling the response of braided composite structures under impact loads [11]. This last CDM model was improved and incorporated into the material libraries of Pam-Crash by Fouinneteau [12].

Matzenmiller's model was adapted and implemented for fabric-reinforced composites in LS-DYNA by Iannucci et al. [15], which was later improved by means of the Crack Band methodology. The Crack Band methodology adjust the energy dissipated for each finite element [16]. Furthermore, Bohm et al. extended Matzenmiller's model to 2D and 3D fabric-reinforced composites [14].

Miamí et al. [22, 23] proposed a Continuum Damage Model for the prediction of the onset and evolution of intralaminar failure mechanisms and the collapse of structures conformed with fibre-reinfroced plastic laminates, based on a simplification of the LaRC04

failure criteria. On the other hand, Martín-Santos et al. [1] developed a CDM model for the simulation of fabric-reinforced composites. Both models incorporate Bažant's Crack Band Model [16] for each intralaminar failure mode considered in the model. They were implemented and validated in ABAQUS/Explicit FE code using a user-subroutine. The accuracy of these models were assessed by simulating open-hole specimens under quasi-static tensile loading conditions.

Chapter 3

Continuum Damage Mechanics

3.1 State of the art

This section is concerned with the application of Continuum Damage Mechanics theory (CDM) to the damage analysis of fibre-reinforced composites. Most of the software used today in crash analysis of composites is based on macro-mechanics and are not able to differentiate all of the failure modes on a micro-scale level. Continuum damage mechanics simply represents all the failure modes by the effect they have on the meso-scale (lamina level) behaviour of the material. Thus, failure mechanisms and their coupling under complex stress states of an elementary ply are considered.

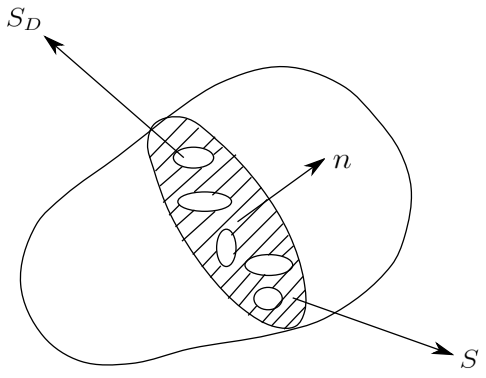

Figure 3.1: Representative volume element for damage mechanics.

In One-Dimensional Damage Mechanics, when a composite rod of section S, unloaded and free of any damage, is subject to a sufficiently large load P, damage appears and several different failure modes can be present. In CDM, damage or degradation is initiated when the strain or stress exceeds the initial damage threshold (ε_0, σ_0) and it is reperesented by a state variable d, called damage variable, which represents the loss of stiffness and the reduction of area due to accumulation of damage,

$$d = 1 - E_d/E = S_d/S \qquad 0 \leq d \leq 1, \tag{3.1}$$

where E_d is the Young's modulus after damage, E is the undamage Young's modulus, S_d is the damaged cross-section area and S is the initial cross-section area (Figure 3.1). The effective stress tensor ($\bar{\sigma}$) corresponds to the undamaged configuration ($d = 0$), written in terms of Hooke's law is,

$$\bar{\sigma} = E\varepsilon. \tag{3.2}$$

where ε is called the strain tensor and it indicates the percentage deformation of an infinitesimal element. Therefore, taking into account the increase of effective stress and the decrement of stiffness caused by damage, the apparent stress is,

$$\sigma = (1-d)E\varepsilon = (1 - S_d/S)E\varepsilon = E_d\varepsilon = (1-d)\bar{\sigma}. \tag{3.3}$$

Damage is initiated when the stress state (σ) is higher than the threshold (σ_0), that is a material property characteristic of each damage mechanism. Therefore, while the stress field in the material is below a threshold, the material is in the elastic domain ($\sigma \leq \sigma_0$ and $\varepsilon \leq \varepsilon_0$) and thus, no damage occurs. For some materials, the threshold changes once the non-linear behaviour is onset, since the elastic domain may evolve as hardening, softening or even showing both of them in their useful life. After damage is onset, the increase of the strain leads to an increase on the stress threshold. A stress threshold increases for material with hardening and it decreases for materials with softening, i.e. both of them lead to a reduction on stiffness. On the other hand, unloading does not produce healing and during unloading the damage does not increase either, i.e. $\dot{d} = 0$. In Figure 3.2 can be observed a general stress-strain law with damage.

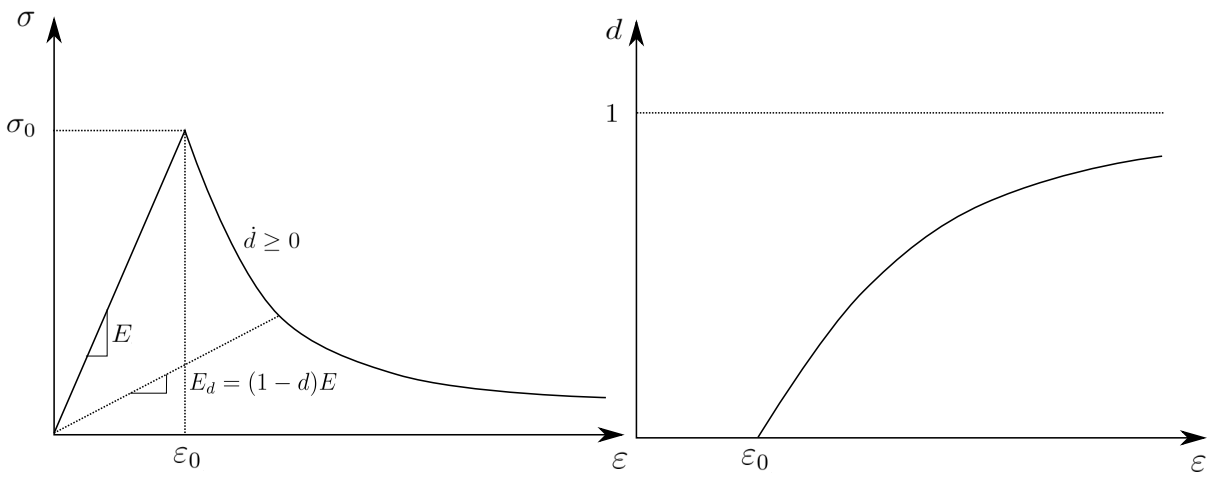

Figure 3.2: Uniaxial continuum damage model.

In general, energy is absorbed by two different main mechanisms: inelastic deformation of the material, as hardening, and formation of new surfaces, such as cracks. According to their location, the main failure modes of fibre-reinforced composites are divided in: intra-laminar failure modes, corresponding to fibre and matrix failure, and inter-laminar failure modes, corresponding to delamination between plies. Failure mechanisms in the principal directions at the lamina level are explained below.

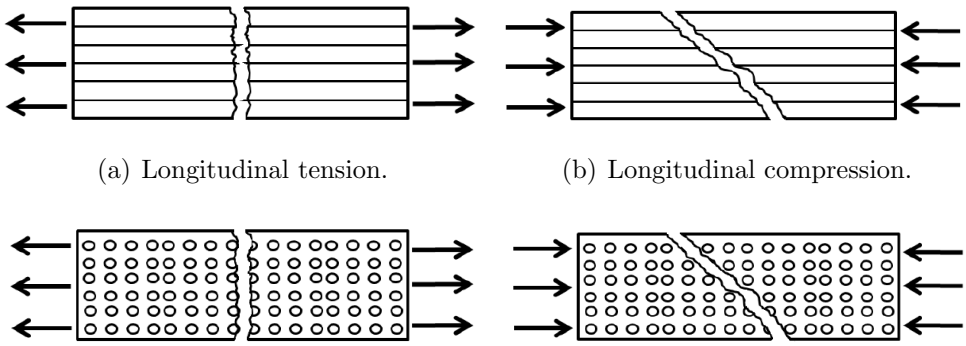

(a) Longitudinal tension. (b) Longitudinal compression.

(c) Transverse tension. (d) Transverse compression.

Figure 3.3: Fibre and matrix failure modes under uniaxial stresses.

Longitudinal tension. In the fibre direction, a ply generally shows elastic-brittle fracture. The initial failure is a fibre break accompanied by some loss of effective fibre length. The behaviour of the composite in the reinforcement direction is influenced by the fibre mechanical properties, volume fraction and configuration. That is, these characteristics take influence on the presence of the different damage mechanisms under tensile loads and thereby, also in the total absorbed energy. Three different damage mechanisms are mainly observed when the material is loaded in the fibre direction: fibre tensile failure, fibre-matrix pull-out and matrix cracking.

Longitudinal compression. When a fibre-reinforced lamina is compressed in the longitudinal direction, different failure modes can occur. The characteristic modes of failure are: fibre micro-buckling with matrix elastic and fully bonded, matrix yielding or interfacial debonding followed by filament microbluckling, panel microbuckling, shear failure and ply separation by transverse tension. In models that consider fibre bluckling, it is assumed that buckling of the fibres initiates a process that leads to the collapse of the material. If the fibres are densely packed, the buckling of fibres occur in-phase, in this mode the matrix exhibits mostly shear strains and shear failure occurs, forming kink bands. Shear failure is typically triggered at imperfections, like voids in the matrix or because of the misalignment of the fibres.

Transverse tension. In the transverse direction under tensile load, for unidirectional composites failure is dominated by the high strain concentration in the matrix. The primary failure modes are tensile matrix failure and fiber debonding, in this case the fracture plane is perpendicular to the loading in unidirectional tests.

Transverse compression. The primary failure modes under compression in the transverse direction are compressive failure and shear failure in the matrix. Due to shear failure, as opposed to failure modes in the transverse direction under tensile, the fracture plane is most often at an angle to the loading direction. Sometimes failure is accompanied by fiber debonding in unidirectional tests.

On the other hand, regarding inter-laminar failure in fibre-reinforced composites, *Delamination* between plies is caused by interlaminar stresses in conjunction with the typically very low through-thickness strength producing a fracture surface without the need to

break fibres. A delamination crack is often preceded by a matrix crack who has propagated through a ply until it has reached the fibers of an adjacent ply. This inter-laminar failure mode is often found in specimens who have been subject to bending, due to predominant out-of-plane shear stresses. In laminates under in-plane compression, the delaminated layers may buckle and propagate due to interaction between delamination growth and buckling.

The onset and evolution of the different damage mechanisms presented above, from the initiation of damage until the total degradation, are defined as constitutive laws based on the Cohesive Zone Model (CZM). The CZM describes the separation between internal surfaces in the material by means of traction-displacement laws. It links the micro-structural failure mechanisms to the continuum deformation field. The CZM offers an alternative way to reproduce failure in materials or along material interfaces: the stress state between the cohesive surfaces evolves according to a predefined softening law, which is called the cohesive law. The cohesive zone model is representative of a crack tip extension, but not the strain field of the material surrounding it. Cohesive laws, then, do not show any displacement before damage is onset. As the cohesive surfaces separate, different traction-separation laws can be considered, reproducing the loss of stiffness in the crack propagation plane. Then, subsequently when the force able to be supported by the cohesive zone model is reduced to zero, the complete separation of the faces bounded by the CZM is achieved. The area under the traction-displacement curve is equal to the energy needed for separation of a surface unit, called fracture toughness ($\mathcal{G}_M$).

There are two approaches to develop a cohesive law: its measurement by means of experimental methods or its design by predefined assumptions and estimated theoretical parameters. Thus, a cohesive zone model is characterized by the shape of the traction-displacement curve, which generally can be modelled as constant, linear or exponential (Figure 3.4), and the value of the cohesive parameters determined from experimental data using indirect methods [24, 37, 38]. Thus, the material fracture properties are mainly characterized by three parameters: fracture energy, uniaxial strength limit and width of the crack band.

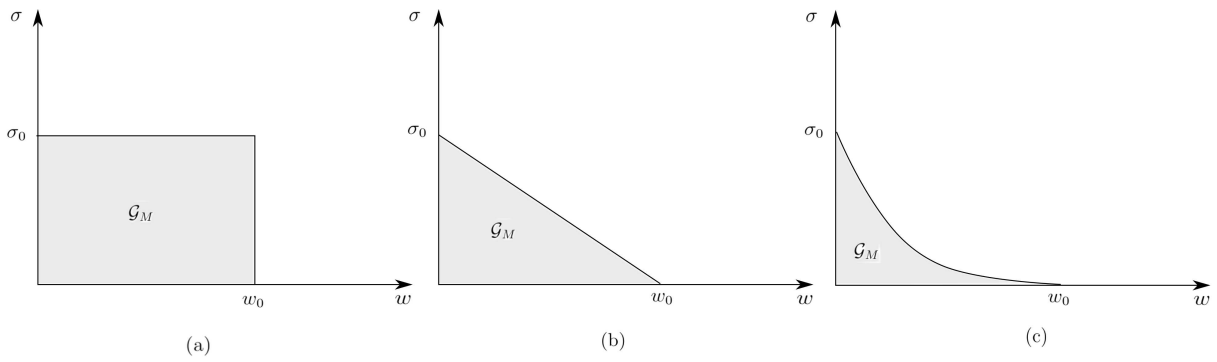

Figure 3.4: Different types of cohesive laws.(a) Constant. (b) Linear. (c) Exponential.

Moreover, the shape of the softening law plays a fundamental role in the prediction of fracture in problems where the process zone length may be large relative to other length scales [18, 19, 20]. In order to take into account different failure mechanisms, several cohesive laws have been proposed by different authors [22, 23, 21]. A linear softening law is insufficient to account for the multiple damage mechanisms and the toughening due to fibre dridging and fiber pull-out, a bilinear softening law provides a more accurate approximation for quasi-brittle materials such as concrete or composite materials [24].

3.2 Constitutive formulation

In this section, a CDM model for fabric-reinforced composite plies under a shell formulation is presented, based on the model presented by Martín-Santos et al. [1]. The model includes a cohesive law-based formulation to describe the degradation of the mechanical properties for the implemented damage mechanisms and an isotropic hardening plasticity for the in-plane shear behaviour.

A plane-stress state is assumed in order to define the model in the plane of shell elements. In contrast to many other engineering materials, such as metals, composites are not isotropic. A single lamina of fibre reinforced composite behaves as an orthotropic material. That is, the properties differ in the three perpendicular directions. For unidirectional composites, the properties in all transverse directions to the fiber are the same, providing these materials with orthotropic symmetry. The intersection of these three planes defines three axes that coincide with the fibre direction (x_1'), the thickness

coordinate (x_3') and a third direction perpendicular to the other two (x_2'), which can be aligned with the matrix, for unidirectional composites, or the fibre with the weakest properties, for fabric-reinforced composites. Thus, for fabric-reinforced composites direction 1 is aligned with the weft tows, corresponding to the fibres with the strongest properties, and direction 2 is aligned with warp tows (Figure 3.5).

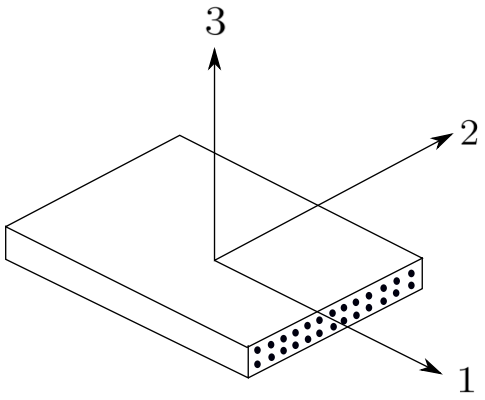

Figure 3.5: Axis.

3.2.1 Complementary energy and elastic response

The elastic material formulation of the complementary free energy density ($\rho_0\psi$) is related to the Helmholtz free energy function ψ. This function must be positive definite and zero at the origin with respect to the free variables, which are stresses and strains.

$$\rho_0\psi = \frac{1}{2}(\varepsilon_{ij} - \varepsilon_{ij}^p)C_{ijkl}(\varepsilon_{kl} - \varepsilon_{kl}^p) = \frac{1}{2}\varepsilon_{ij}^e C_{ijkl}\varepsilon_{kl}^e = \frac{1}{2}\varepsilon_{ij}^e\sigma_{ij} \tag{3.4}$$

For the proposed constitutive model the scalar funcion of the complementary free energy density is defined as,

$$\rho_0\psi = \frac{\sigma_{11}^2}{2(1-d_1)E_{11}} + \frac{\sigma_{22}^2}{2(1-d_2)E_{22}} + \frac{\sigma_{12}^2}{2G_{12}} - \frac{\nu_{12}}{E_{11}}\sigma_{11}\sigma_{22} + \sigma_{12}\varepsilon_{12}^p \tag{3.5}$$

where σ_{11}, σ_{22} and σ_{12} are components of the stress tensor, E_{11} and E_{22} are the elastic modulus, G_{12} is the in-plane shear modulus, ν_{12} is the Poisson's coefficient and ε_{12}^p is the plastic component of the shear strain. The damage variables d_1 and d_2 are associated with the weft and warp directions, respectively, for fabric-reinforced composites. The proposed

constitutive model does not include the degradation of the properties under shear stresses since matrix damage is not considered a catastrophic mode of failure.

A material is elastic if for all closed paths of deformation the rate of free energy is equal to zero, i.e., if the deformation of the material does not entail dissipation. Since damage is considered, in order to ensure the irreversibility of the damage process, the energy dissipated must be defined as follows,

$$\mathcal{D} = \rho_0 \dot{\psi} - \dot{\boldsymbol{\sigma}} : \boldsymbol{\varepsilon} \geq 0$$

$$\mathcal{D} = \rho_0 \frac{\partial \psi}{\partial \varepsilon_{12}^p} \dot{\varepsilon}_{12}^p + \rho_0 \frac{\partial \psi}{\partial d_1} \dot{d}_1 + \rho_0 \frac{\partial \psi}{\partial d_2} \dot{d}_2 + (\rho_0 \frac{\partial \psi}{\partial \boldsymbol{\sigma}} - \boldsymbol{\varepsilon}) : \dot{\boldsymbol{\sigma}} \geq 0 \qquad \forall \dot{\sigma} \tag{3.6}$$

Eq. 3.6 holds for every rate of stress only if the term between brackets is equal to zero. In consequence, the constitutive equation is obtained,

$$\boldsymbol{\varepsilon} = \rho_0 \frac{\partial \psi}{\partial \boldsymbol{\sigma}} = \mathbf{H} : \boldsymbol{\sigma} + \varepsilon_{12}^p \tag{3.7}$$

where $\mathbf{H}$ is the compliance tensor, represented in Voigt notation as follows,

$$\mathbf{H} = \begin{bmatrix} \frac{1}{(1-d_1)E_{11}} & -\frac{\nu_{12}}{E_{11}} & 0 \\ -\frac{\nu_{12}}{E_{11}} & \frac{1}{(1-d_2)E_{22}} & 0 \\ 0 & 0 & \frac{1}{G_{12}} \end{bmatrix} \tag{3.8}$$

Taking into account the different behaviours of the tensile and compressive mechanisms for each fibre direction, NT and NC respectively, the damage variables are defined as,

$$d_N = d_{NT} \frac{\langle \sigma_N \rangle}{|\sigma_N|} + d_{NC} \frac{\langle -\sigma_N \rangle}{|\sigma_N|} \quad N = 1, 2 \tag{3.9}$$

where N denotes the principal direction and $\langle - \rangle$ are the Macaulay brackets, defined as,

$$\langle x \rangle = \begin{cases} x & x > 0 \\ 0 & x < 0 \end{cases} \tag{3.10}$$

3.2.2 Damage threshold and activation functions

As it has been explained in Section 3.1, the state of damage is unchanged along a path of strain inside the elastic domain. The elastic domain is defined by the loading criterion in stress or strain domains. For the model presented in this work, the loading functions that define the elastic domain of the material depend on the strain tensor and the material properties. In order to take into account the different failure modes, the following loading functions are defined,

$$\begin{aligned} \phi_{1T} &= \frac{\langle \bar{\sigma}_{11} \rangle}{X_{1T}}; \qquad \phi_{1C} = \frac{1}{X_{1C}} \left(\langle -\bar{\sigma}_{11} \rangle + \eta_{1T} \bar{\sigma}_{22} + \eta_{1S} |\bar{\sigma}_{12}| \right) \\ \phi_{2T} &= \frac{\langle \bar{\sigma}_{22} \rangle}{X_{2T}}; \qquad \phi_{2C} = \frac{1}{X_{2C}} \left(\langle -\bar{\sigma}_{22} \rangle + \eta_{2T} \bar{\sigma}_{11} + \eta_{2S} |\bar{\sigma}_{12}| \right) \end{aligned} \tag{3.11}$$

where X_{1T}, X_{1C}, X_{2T} and X_{2C} are the ultimate strengths for each direction and damage mechanism, and η_{1T}, η_{1S}, η_{2T}, η_{2S} are non-dimensional coupling factors that define the biaxial strengthening behaviour. The values of the non-dimensional coupling factors can be obtained by perfoming biaxial tests on thickness-tapered cruciform specimens in order to define the failure envelope [25]. The effective stress tensor is defined as,

$$\bar{\boldsymbol{\sigma}} = \mathbf{C}_0 : \boldsymbol{\varepsilon}^{\boldsymbol{e}}, \tag{3.12}$$

where $\mathbf{C}_0$ corresponds to the undamaged stiffness tensor. The stiffness tensor $\mathbf{C}$ is obtained by means of the inverse of the compliance tensor (Eq. 3.13). Therefore, $\mathbf{C}_0$ is obtained when d_1 and d_2 are equal to zero.

$$\mathbf{H}^{-1} = \mathbf{C} = \begin{bmatrix} \frac{E_{11}(1-d_1)}{1-\nu_{12}\nu_{21}(1-d_1)(1-d_2)} & \frac{E_{11}\nu_{21}(1-d_1)(1-d_2)}{1-\nu_{12}\nu_{21}(1-d_1)(1-d_2)} & 0 \\ \frac{E_{22}\nu_{12}(1-d_1)(1-d_2)}{1-\nu_{12}\nu_{21}(1-d_1)(1-d_2)} & \frac{E_{22}(1-d_2)}{1-\nu_{12}\nu_{21}(1-d_1)(1-d_2)} & 0 \\ 0 & 0 & G_{12} \end{bmatrix} \tag{3.13}$$

The different failure modes can be observed in the tensile and compressive loading functions (Eq. 3.11). In the tensile related failure mechanisms only the effective stress of the corresponding direction is considered since no coupling effects are present. Whereas in the compressive related mechanism, the rest of components in the effective stress tensor are taken into account, in order to consider the influence of the complex stress field in the collapse of the material due to fibre micro-buckling.

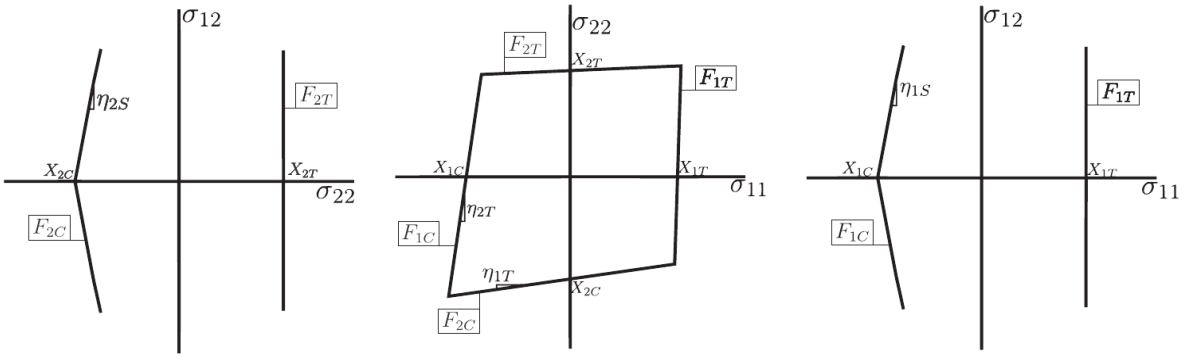

Figure 3.6: Failure surfaces for the model presented by Martin-Santos et al. [1].

The damage thresholds are internal variables that measure the size of the elastic region. The elastic range for each direction and mechanism is bounded by the loading functions previously defined, i.e. is bounded by four surfaces: 1T, 1C, 2T and 2C. Therefore, each loading function have its own threshold r_M, which set the maximum value that the loading functions can achieve before damage is initiated. Once the loading function takes a value bigger than its damage threshold, damage evolves and the value of the damage threshold is updated. For this model, the crack closure mechanism under compression is implemented through the internal variables, since tensile damage is not taken into account

for compressive stresses, while the tensile mechanisms take into account both the tensile and compressive loading functions. Therefore, the damage thresholds, r_{NT} and r_{NC}, are computed under an explicit integration as follows:

$$r_{NT} = \max_{s=0,t} \{1, \phi^s_{NT}, \phi^s_{NC}\} \quad ; \quad r_{NC} = \max_{s=0,t} \{1, \phi^s_{NC}\} \qquad N = 1, 2 \tag{3.14}$$

When the related variable in the effective stress tensor reaches the value of the ultimate strength (X_{NT}, X_{NC}), damage is onset and the internal variables increase from a value of 1 to the value of the current loading function in order to define the new threshold for damage evolution. The evolution of the damage thresholds variables are governed by the consistency condition, $\dot{F}_M = 0$, which relates the evolution of the thresholds to the one for the damage variables, where F_M are the damage activation functions defined as,

$$F_M = \phi_M - r_M \geq 0 \qquad M = 1T, 1C, 2T, 2C \tag{3.15}$$

Since r_M set the maximum value that the loading functions can achieve before damage is initiated, when $\phi_M < r_M$, i.e. $F_M < 0$, there is an elastic response at that point in the material. The degradation of the material is propagated when the effective stress state is on the failure surface ($F_M = 0$).

3.2.3 Damage evolution

For this model, the cohesive laws defining the damage evolution in a composite ply are described as a bilinear relation between the tractions and the displacement [1]. The first stage represents the processes ocurring in the vicinity of the crack tip. The second stage is used to simulate the energy release caused by other effects, such as fibre bridging or pull-out mechanisms. An example of a bilinear cohesive law is shown in Figure 3.7(a). As can be observed the parameters that define the bilinear cohesive law are four:

- X_M is the ultimate strength.

- f_{X_M} is the factor for determining the pull-out stress ($f_{X_M} X_M$).

- H_M is the slope of the first stage of the cohesive law.

- $\mathcal{G}_M$ is the fracture toughness.

Fibre-reinforced composites exhibit a strong size effect, which consists in a mismatch between the size dependence of the energy release rate and the rate of energy consumption by fracture. The convergence of the solucion through successive mesh refinement must be ensured. Therefore, Bažant's Crack Band Model [16] is employed in order to simulate the size effect and to ensure the objectivity of the numerical model. It consists in a simple approach in which the size of the elements in the crack band is considered to be a material property, in that way the energy dissipated ($\mathcal{G}_M$) is adjusted for each finite element. Thus, a characteristic length (l_c), internally obtained by the FE software used, by means of the length of the sizes of the element, is introduced:

$$g_M = \frac{\mathcal{G}_M}{l_c}, \qquad M = 1T, 1C, 2T, 2C \tag{3.16}$$

The continuum formulation is characterized by two constitutive relations: a traction versus displacement jump relation across a specified set of cohesive surfaces and a volumetric law that relates stress and strain. That is, the traction-displacement cohesive law must be adapted to a volumetric law in order to be implemented in finite elements (Figure 3.7). The volumetric law is defined by the slope and the y-intercept terms of the two degradation stages as follows,

$$\sigma = A_{IM}\varepsilon + B_{IM} \begin{cases} I = 1 & \text{for } 1 < r_M \leq r_{c_M} \\ I = 2 & \text{for } r_M > r_{c_M} \end{cases} \tag{3.17}$$

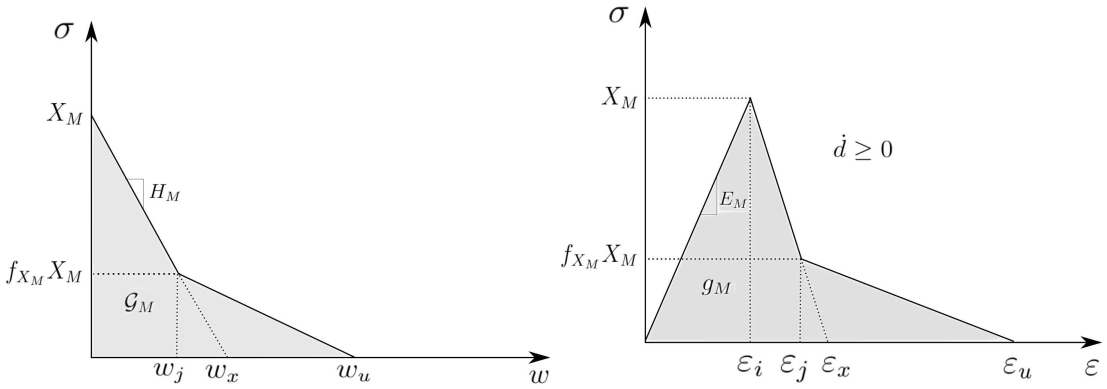

(a) Stress-displacement. (b) Stress-strain.

Figure 3.7: Cohesive bilinear law and its equivalent volumetric implementation.

The values of A_{IM} and B_{IM} can be obtained in terms of the variables that appear in Figure 3.7:

$$\varepsilon_i = \frac{X_M}{E_M}, \qquad \varepsilon_j = \frac{f_{X_M} X_M - B_{1M}}{A_{1M}},$$
$$\varepsilon_x = \frac{2X_M^2}{l_c X_M H_M}, \qquad \varepsilon_u = \frac{2(\mathcal{G}_M H_T - X_M^2(1 + f_{X_M}))}{l_c f_{X_M} X_M}.$$

$$A_{1M} = \frac{X_M}{\varepsilon_i - \varepsilon_x}, \qquad B_{1M} = -\varepsilon_x A_{1M}, \tag{3.18}$$
$$A_{2M} = \frac{f_{X_M} X_M}{\varepsilon_j - \varepsilon_u}, \qquad B_{2M} = -\varepsilon_u A_{2M}. \tag{3.19}$$

A critical value for the internal variables at which the second stage begins is defined:

$$r_{c_M} = \frac{1 - \left[\left(1 - \frac{E_M}{H_M l_c}\right)(1 - f_{X_M}) + f_{X_M} \nu_{12} \nu_{21}\right]}{1 - \nu_{12}\nu_{21}} \tag{3.20}$$

Finally, taking into account the definition of damage in Eq. 3.3, the damage variables for each mechanism are computed as follows,

$$d_M = \frac{X_M r_M (1 - \frac{A_{IM}}{E_M}) - B_{IM}}{X_M r_M + B_{IM} \nu_{21} \frac{\alpha}{1 - \nu_{12}\nu_{21}}} \begin{cases} I = 1 & \text{for } r_M \leq r_{c_M} \\ I = 2 & \text{for } r_M > r_{c_M} \end{cases} \tag{3.21}$$

where $\alpha = \nu_{12} - \eta_{MT}$ for the compressive laws and $\alpha = \nu_{12}$ for the tensile laws.

According to Miamí et al. [23], in order to prevent snap-back in the stress-strain relation, the element size must fulfill certain condition. The elastic energy of an element at the onset must be lower than or equal to the fracture toughness. That is, the caracteristic length of the element must be smaller than the relationship $\frac{E_M}{H_M}$.

3.2.4 Shear isotropic hardening

For fibre-reinforced composites in which the fiber has a much higher modulus than the matrix, the shear behaviour is controlled entirely by the properties of the matrix deforming under the geometrical contraints imposed by the fibres [4]. Thus, the inelasticity under shear stresses is taken into account through the use of an isotropic hardening approach.

In a perfectly plastic case, once the stress reaches the yield point (S_{LP}), plastic deformation ensures as long as the stress is maintained at the yield point. Composite materials show hardening plasticity: once yield occurs, the stress needs to be continually increased in order to drive the plastic deformation. The isotropic hardening occurs when the yield surface maintains the same shape but it is expanded with increasing stress. The part of strain caused by means of the hardening mechanism is the Plastic strain (ε_{12}^p), which remains pemanent after the material is unloaded. Elastic strain (ε_{12}^e), once the hardening is onset, is the part of strain capable to store internal energy and thus, be recovered when the material is unloaded. Total strain is the sum of elastic strain and plastic strain, $\varepsilon_{12} = \varepsilon_{12}^e + \varepsilon_{12}^p$. When hardening occurs the value of the yield stress changes, for this reason in plasticity models an internal isotropic hardening variable is used in order to keep track of the total change in plastic strain (ε_{12}^i). A yield function F_p controls the onset and propagation of the plastic behaviour, defined as:

$$F_p = |\bar{\sigma}_{12}| - \left(S_{LP} + \varsigma_E \left[1 - e^{-\left|\varsigma_E^T \varepsilon_{12}^i\right|}\right] + \varsigma_L \varepsilon_{12}^i\right) \leq 0 \tag{3.22}$$

where S_{LP}, ς_E, ς_E^T and ς_L are the parameters defining the isotropic hardening law. Figure 3.8 shows a scheme of the isotropic hardening law used in this model in which σ_{12} follows the expression in Eq. 3.23.

$$\sigma_{12} = S_{LP} + \varsigma_E \left[1 - e^{-\left|\varsigma_E^T \varepsilon_{12}^p\right|}\right] + \varsigma_L \varepsilon_{12}^p \tag{3.23}$$

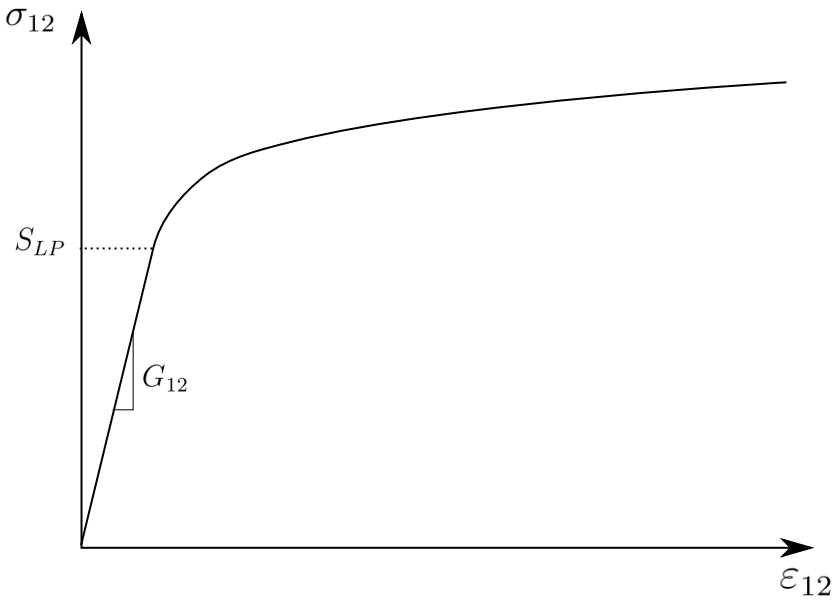

Figure 3.8: Shear isotropic hardening law.

The evolution of plastic strain in plasticity algorithms is called a flow rule. In this model the flow rule takes the form $\dot{\varepsilon}_{12}^p = \dot{\varepsilon}_{12}^i sign(\varepsilon_{12}^e)$. As the plastic strain increases, ε_{12}^i is updated and the yield condition is computed. If F_p is negative it means that the current level of stress is below the current yield threshold and only the elastic strains are increasing. If F_p is positive, the current level of stress is above the current yield limit and elastic and plastic strains are increasing. However, $F_p > 0$ is not allowed, therefore, ε_{12}^i, ε_{12}^p and ε_{12}^e must be updated such that F_p is equal to zero. This scheme will be explained in more detail in Section 4.2.

Chapter 4

Numerical formulation

The objective of this chapter is to briefly present basic concepts regarding the finite element analysis. For this, in the first section some of the basis of the Finite Element Method (FEM) are presented, for the understanding of the solution process that commercial softwares using with this discretization method follow. The second section describes the steps needed for the implementation in FORTRAN of the Continuum Damage Model for fabric-reinforced composites presented in the previous section.

4.1 Overview of FEM

The Finite Element Method (FEM) is a numerical procedure used for the analysis of complex problems in different fields of engineering, such as civil engineering, mechanical engineering, nuclear engineering, biomedical engineering, hydrodynamics, heat conduction, geo-mechanics, etc. It is a powerful tool to approximate solution of differential equations describing different physical processes. The process to carry out in order to model real complex problems using mathematical tools and computers can be summarized in the scheme shown in Figure 4.1.

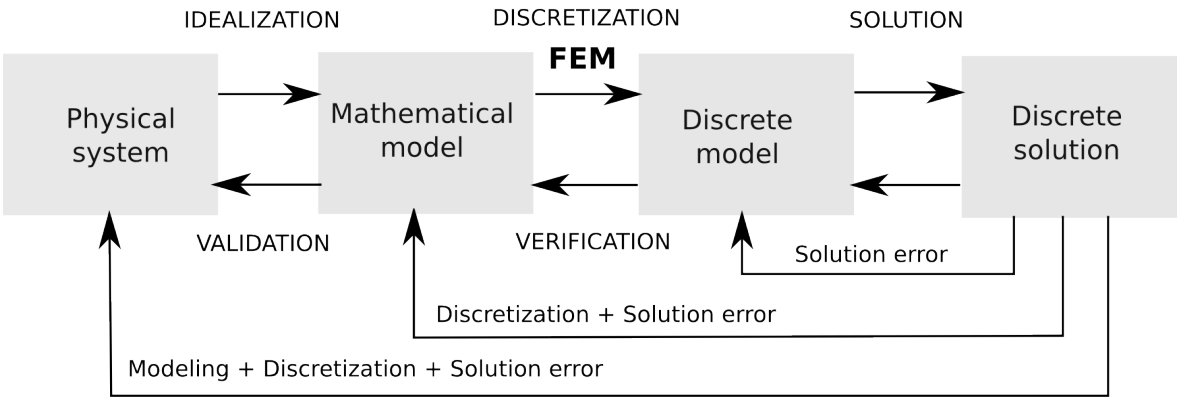

Figure 4.1: Process steps to model real complex problems.

As can be observed, the first step is to discover mathematical relationships that describe the behaviour of the physical system, which normally are ordinary and partial differential equations. Since the equations are most of the time impossible to solve with analytical methods, they have to be mapped from a continuous (infinite dimensional) space into a discrete (finite dimensional) space. This process is called discretization and it is carried out through FEM. The domain is discretized in smaller domains, called finite elements. The method approximates values of the unknowns at a discrete number of points over the domain called nodes.

Every element is described by its nodal points. Therefore, the number of nodes per element depends on:

- The dimension of the element: Depending on the problem context, elements can be 1D, 2D or 3D.

- Type of approximation: Frequently, nodes are chosen to be the corners of the element. These elements are called linear elements, since they use a linear approximation of the displacement field over the domain of the element. However, elements with higher order of approximation can be used. In the case of quadratic elements, nodal points are also defined on the edges of the element.

- Geometry: Depending on the complexity of the problem geometry, different element geometries may be chosen (Figure 4.2).

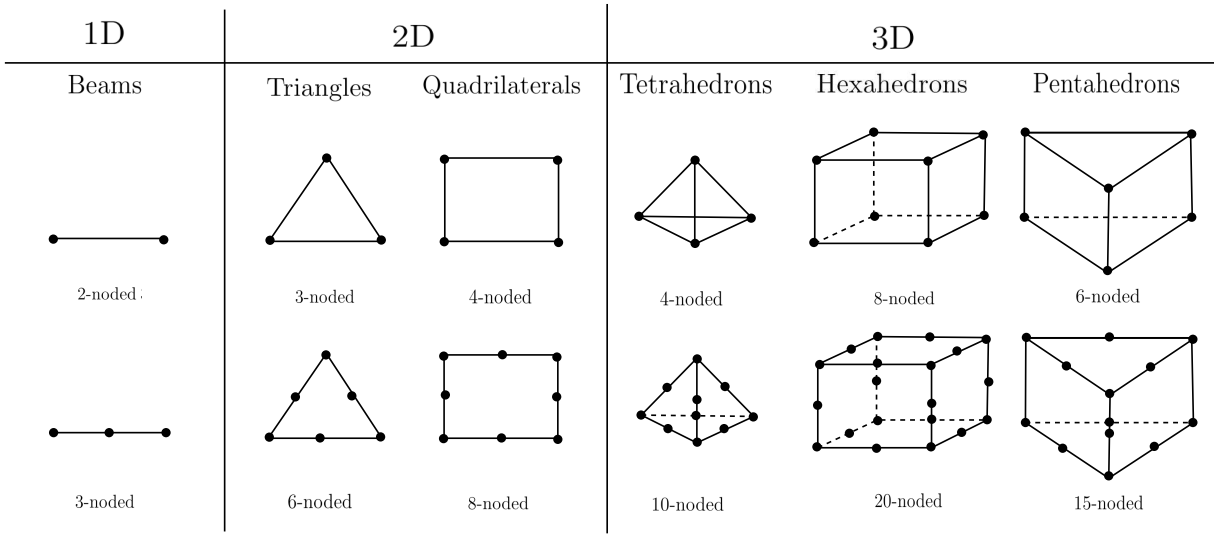

Figure 4.2: Basic elements.

The success of the FEM is based on the basic finite element procedures used:

1. The formulation of the problem in variational form. A strong form of the governing equations of a physical system, along with boundary conditions, states the conditions at every point over a domain that a solution must satisfy. A Dirichlet or essential boundary condition specifies the values a solution needs to take on the boundary of the domain, whereas, a Neumann or natural boundary condition specifies the values that the derivative of a solution needs to take on the boundary of the domain.

The formulation of the problem in variational form consist in the reformulation of the partial differential equation (strong form) into an equivalent form, and this form has the weak form. In order to establish the weak form, the residual of the PDE is multiply by a weighting function w vanishing on the Dirichlet boundary Γ_D, and the integral over the domain Ω is set equal to zero. Then, the equation is integrated by parts using the Neumann boundary conditions.

2. The finite element discretization of this formulation. That is, representing the approximate solution û as a linear combination of polynomial basic functions N_i defined on a given mesh. One of the most popular and powerful numerical techniques is the Galerkin method, which consist in using w in terms of the shape functions N_i. Therefore, the functions û and N_i substitute u and w in the weak formulation, respectively.

3. The effective solution of the resulting finite element equations. The formulation of the problem results in a system of algebraic equations for steady state problems:

$$\mathbf{Ku} = \mathbf{f} \tag{4.1}$$

where **K** is the stiffness matrix, **u** is the vector of unknowns and **f** the external forces vector.

Whereas for transient problems, after the spatial discretization, the formulation results in a system of ordinary differential equations in time:

$$\mathbf{Mu"} + \mathbf{Cu'} + \mathbf{Ku} = \mathbf{f} \tag{4.2}$$

where **M** is the mass matrix, **C** is the damping matrix and **K** is the stiffness matrix. **u"**, **u'** and **u** are the acceleration, velocity and displacement vectors, respectively. **f** is the external forces vector.

This system can be discretized in time using various time integration methods. The aim of the integration methods used for the solution of transient problems is to satisfy the equation of motion at discrete time invervals. But, the time step Δt, does not need to be constant through the integration process. Time integration methods can be clasified as *explicit* and *implicit*. An *explicit analysis* computes the current solution in time (t_{n+1}) from the known values of the solution calculated in the previous time step (t_n). Since this method is conditionally stable, very small time steps need to be used in order to satisfy the condition of numerical stability. Whereas, in an *implicit analysis* the calculation of the current solution in time is based on the solution calculated in the previous time step, but also considers the stress state in the current step. Therefore, implicit integration schemes become unconditionally stable, but their application implies the resolution of a system of equations at every time step. This can lead to convergence problems in simulations when

non-linearities are present. For linear problems, the solution remains stable even if large time steps are taken.

In general, explicit methods are used in case of impact loadings and crash tests because of its high non-linearity and the duration of the impact event, that is usually small. The time step in these analysis must be smaller than the Courant time step, which is defined as the time it takes a sound wave to travel across an element:

$$C = \frac{l_c}{c} = l_c\sqrt{\frac{\rho}{E}}, \tag{4.3}$$

where C is the Courant number, l_c is the caracteristic length of the elemet, ρ is the density of the material and c is the wave speed. That is, the time increment to obtain a stable integration increases proportionally with respect to the element size. During the simulation, the stable time increment is equal to the smallest time increment computed for each element of the model.

In this master thesis, a software based on the FEM algorithm is used. PAM-CRASH is a commercial CAE software package from ESI Group used for crash simulation and the design of occupant safety systems, primarily in the automotive industry. It is a non-linear explicit finite element dynamic analysis software which use a Lagrangian formulation with a FE mesh fixed in the material. It offers different structural and continuum elements as beams, shells, membranes and solids, allowing the modelling of complex geometries. For the purpose of the simulation of continuous fibre reinforced composite crash events, PAM-CRASH contains the bi-phase and the matrix fracturing multi-layered composite thin shell model, among others. Regarding the explicit analysis, the equations of motion are integrated in time explicitly using central differences and the time step is continually being updated during the simulation in order to approach the computed stable solution time step. In addition, the user can define some time step control cards. In the simulations performed in this thesis the following control cards will be used: initial time step, stiffness scale control, initial mass scaling, nodal time step, dynamic mass scaling and shell time step criterion selection. On the other hand, additional external forces are introduced in order to resist penetration and control sliding, called penalty forces, very important for contact in the structure in crash analysis.

4.2 Numerical implementation

In this section the steps needed for the numerical implementation of the constitutive model are presented. Constitutive laws in PAM-CRASH are specified using FORTRAN routines which are compiled to the dynamic libraries called by the solver. FORTRAN is a high-level language useful for a wide variety of applications: number crunching, scientific, mathematical, statistical and engineering type procedures. Its natural way of expressing complex mathematical functions makes FORTRAN especially suited to numerical computation and scientific computing.

A given geometry is discretized by the finite element method. For this, a displacement-based finite element formulation is used, i.e. the displacements are the unknown variables which have to satisfy the boundary conditions. Once the displacements have been determined through an explicit scheme, strains are computed in a similar way through the strain-displacement matrix. The stresses are calculated for each element through the implemented constitutive laws at each Gauss integration point. Therefore, at calculation time t for each finite element and for each time step, the known variables are the total strains, the associated strain increments and the set of variables calculated at the previous time step $t-1$.

The complete algorithm used for the integration of constitutive equations described in Section 3.2 is shown next. At time t and at the Gauss integration point of an element:

1. The total strains and the associated strain increments are obtained from the FEM code:

$$\boldsymbol{\varepsilon_{(t)}} = (\varepsilon_{11}, \varepsilon_{22}, \varepsilon_{33}, \varepsilon_{12}, \varepsilon_{23}, \varepsilon_{13})^T \quad \boldsymbol{\Delta\varepsilon_{(t)}} = (\Delta\varepsilon_{11}, \Delta\varepsilon_{22}, \Delta\varepsilon_{12}, \Delta\varepsilon_{23}, \Delta\varepsilon_{13}, \Delta\varepsilon_{33})^T$$

2. The undamaged stiffness matrix $\mathbf{C}_0$ and the effective stress $\boldsymbol{\bar{\sigma}_t}$ are computed using Equations 3.13 and 3.12, respectively.

$$\boldsymbol{\bar{\sigma}_{(t)}} = (\sigma_{11}, \sigma_{22}, \sigma_{12}, \sigma_{23}, \sigma_{13})^T$$

3. A return-mapping algorithm is used to solve the isotropic hardening plasticity for the variables ($\varepsilon^e_{12_{(t)}}$, $\varepsilon^p_{12_{(t)}}$, $\varepsilon^i_{12_{(t)}}$) with the following steps:

Step 1. Compute the elastic strain at time t:

$$\varepsilon^{e}_{12_{(t)}} = \varepsilon_{12_{(t)}} - \varepsilon^{p}_{12_{(t-1)}}$$

Step 2. Compute the effective stress at time t:

$$\bar{\sigma}_{12_{(t)}} = C_{33}\varepsilon^{e}_{12_{(t)}}$$

Step 3. Compute $F_{p_{(t)}}$:

$$F_p = \left|\bar{\sigma}_{12_{(t)}}\right| - \left(S_{LP} + \varsigma_E\left[1 - e^{-\left|\varsigma_E^T \varepsilon^{i}_{12_{(t-1)}}\right|}\right] + \varsigma_L \varepsilon^{i}_{12_{(t-1)}}\right) \geq 0$$

Step 4. If $F_p \leq 0$, the current level of stress is below the yield threshold and only the elastic strains increase (go to *Step 12.*). If $F_p \geq 0$, the current level of stress is outside the yield surface. Therefore, ε^{e}_{12}, ε^{p}_{12}, ε^{i}_{12} must be updated so that $F_p = 0$.

The internal variables are updated by a linearized procedure between two consecutive iterations, k and $k+1$. The equation $F_p = 0$ is solved through the *Newton-Raphson iterative method*. This procedure goes from Step 6 to 11.

Step 6. Initialize iteration counter: $k = 0$

Step 7. While the absolute value of F_p at time t, is greater than a given tolerance.

Step 8. Solve the linearized equation: $F_{p_{(t)}} + DF_{p_{(t)}}\Delta\varepsilon^{i}_{12_{(t)}} = 0$.

Step 9. Update $\varepsilon^{e}_{12_{(t)}}$, $\varepsilon^{p}_{12_{(t)}}$, $\varepsilon^{i}_{12_{(t)}}$

$$\varepsilon^{i}_{12_{(t)}} = \varepsilon^{i}_{12_{(t-1)}} + \Delta\varepsilon^{i}_{12_{(t)}}$$

$$\varepsilon^{p}_{12_{(t)}} = \varepsilon^{p}_{12_{(t-1)}} + \Delta\varepsilon^{i}_{12_{(t)}} sign(\varepsilon^{e}_{12_{(t)}})$$

$$\varepsilon^{e}_{12_{(t)}} = \varepsilon_{12_{(t)}} - \varepsilon^{p}_{12_{(t)}}$$

Step 10. Compute $F_{p_{(t)}} = \left|\bar{\sigma}_{12_{(t)}}\right| - \left(S_{LP} + \varsigma_E \left[1 - e^{-\left|\varsigma^{T}_{E}\varepsilon^{i}_{12_{(t)}}\right|}\right] + \varsigma_L \varepsilon^{i}_{12_{(t)}}\right)$

Step 11. Increment the iteration counter $k = k + 1$ and go to *Step 7.*

Step 12. Finally, compute the shear stress $\sigma_{12_{(t)}} = C_{33}\varepsilon^{e}_{12_{(t)}}$

4. The loading functions (X_{1T}, X_{1C}, X_{2T}, X_{2C}) are computed according to Eq. 3.11. For this, the Macaulay brackets are also implemented. The steps required to update the damage propagation thresholds r_{NT} and r_{NC} (Eq. 3.14) are the following:

   Step 1. $r_{NC_{(t)}} = r_{NC_{(t-1)}}$, $r_{NT_{(t)}} = r_{NT_{(t-1)}}$

   Step 2. $r_{NC_{(t)}} = \phi_{NC_{(t)}}$ if $r_{NC_{(t)}} < \phi_{NC_{(t)}}$

   Step 3. $r_{NC_{(t)}} = 1$ if $r_{NC_{(t)}} < 1$

   Step 4. $r_{NT_{(t)}} = \phi_{NT_{(t)}}$ if $r_{NT_{(t)}} < \phi_{NT_{(t)}}$

   Step 5. $r_{NT_{(t)}} = r_{NC_{(t)}}$ if $r_{NT_{(t)}} < r_{NC_{(t)}}$

   Step 6. $r_{NT_{(t)}} = 1$ if $r_{NT_{(t)}} < 1$

5. The slopes and the y-intersections of the bilineal functions ($A_{1M}, B_{1M}, A_{2M}, B_{2M}$) as well as the critical value for the internal variables (r_{CM}) are computed using Eq. 3.18 and 3.20, respectively.

6. Once the damage propagation thresholds, the bilineal functions and the critical value of the internal variables for damage are computed, the damage ($d_{M_{(t)}}$) is obtained according to Eq. 3.21, with $M = 1T, 1C, 2T, 2C$. When the damage for each

mechanism is computed, the total damage in each direction is obtained as follows, with $N = 1, 2$:

$$d_{N_{(t)}} = \begin{cases} d_{NT_{(t)}} & \varepsilon_{NN_{(t)}} > 0 \\ d_{NC_{(t)}} & \varepsilon_{NN_{(t)}} < 0 \end{cases}$$

7. The stresses are updated with the damage previously computed.

$$\sigma_{11_{(t)}} = \frac{E_{11}(1 - d_{1_{(t)}})}{1 - \nu_{12}\nu_{21}(1 - d_{1_{(t)}})(1 - d_{2_{(t)}})}\varepsilon_{11_{(t)}} + \frac{E_{11}\nu_{21}(1 - d_{1_{(t)}})(1 - d_{2_{(t)}})}{1 - \nu_{12}\nu_{21}(1 - d_{1_{(t)}})(1 - d_{2_{(t)}})}\varepsilon_{22_{(t)}}$$

$$\sigma_{22_{(t)}} = \frac{E_{22}\nu_{12}(1 - d_{1_{(t)}})(1 - d_{2_{(t)}})}{1 - \nu_{12}\nu_{21}(1 - d_{1_{(t)}})(1 - d_{2_{(t)}})}\varepsilon_{11_{(t)}} + \frac{E_{22}(1 - d_2)}{1 - \nu_{12}\nu_{21}(1 - d_{1_{(t)}})(1 - d_{2_{(t)}})}\varepsilon_{22_{(t)}}$$

The constitutive model is able to define different modules for traction and compression in each direction. Therefore, for $N = 1, 2$:

$$E_{NN} = \begin{cases} E_{NT} & \varepsilon_{NN_{(t)}} > 0 \\ E_{NC} & \varepsilon_{NN_{(t)}} < 0 \end{cases}$$

8. End of the integration algorithm

Chapter 5

Aspects of experimental material characterization

In this chapter the material characterization of two fibre-reinforced composite materials is presented: Unidirectional carbon-reinforced composite (CC) and fabric carbon-reinforced composite (TC). For this, the experimental tests performed in order to obtain the material properties are explained below.

5.1 Experimental tests

Fibre-reinforced composites selected for this work are nonhomogeneous orthotropic materials, therefore they require special considerations for determining their physical and mechanical properties. Composite materials define a broad spectrum of materials of widely varying properties. Thus, different test methods are required for different classes of composite materials.

Laminated composites are typically constructed from orthotropic plies (laminaes) containing the fibres. In a macroscopic sense, the lamina is assumed to behave as a homogeneus orthotropic material. As it has been explained before, a state of plane stress is assumed. The subscript 1 indicates the longitudinal direction, being the direction with the strongest properties, i.e. the fibre direction, subscript 2 indicates the in-plane transverse direction, i.e. matrix direction for CC material and the warp tows for TC material and the subscript 3 is the thickness direction of the composite ply.

5.1.1 Tensile, compressive and shear tests

Determination of the tensile strength and stiffness properties of individual laminae is performed by tensile tests. In the fibre direction, a ply generally shows elastic-brittle fracture, whereas in the matrix related mechanisms a ply can show nonlinearity before reaching the maximum stress, due to plasticity. That is, the longitudinal and transverse tensile ultimate strengths (X_{1T}, X_{2T}) are defined as the ultimate values of σ_1 and σ_2 for the 0° and 90° tensile tests, respectively. The tensile elastic modulus E_{1T} and E_{2T} are defined as the initial slope of the stress-strain curve for the 0° and 90° tensile test, respectively. On the other hand, the Poisson's ratios ν_{12} and ν_{21} are obtained as the negative ratio of the transverse to longitudinal strains, i.e. $-\varepsilon_2/\varepsilon_1$, for the 0° and 90° tensile test, respectively.

Compression loading of a composite in the fibre direction involves failure of the matrix and fibre-matrix interface, often exhibited as inclined failure planes. That is, the most important function is carried out by the matrix for CC material. On the other hand, composite laminae under transverse compressive loads usually fail under matrix shear combined with the crushing of the fibres. Meaning that for the CC material, it can present a hardening behaviour before the degradation of their properties. To determine the compressive elastic modulus, E_{1C} and E_{2C}, the initial slopes of the stress-strain curve for the 0° and 90° compressive tests are computed. The ultimate stresses, X_{1C} and X_{2C}, are obtained directly from the stress-strain curve as the ultimate values of σ_1 and σ_2.

An in-plane shear test of a composite material is performed to determine the shear modulus, hardening evolution and shear strength. The shear response of a composite material is commonly nonlinear, and its characterization requires the consideration of the entire stress-strain curve to the 5% of total strain, from where the shear state of stress cannot be ensured. Determination of the lamina shear properties from the tensile test results is driven by means of a stress-strain analysis of the $[\pm 45]_{ns}$ specimen. The in-plane shear modulus, G_{12} is obtained establishing the slope of the initial portion of the shear stress-strain curve. The parameters for the hardening description are extracted by means of the adjustement of the $\sigma(\varepsilon^p_{12})$ curve. The ultimate shear stress, X_{SH}, corresponds to the maximum value of the shear stress.

5.1.2 Compact tension test

The use of Linear Elastic Fracture Mechanics (LEFM) to predict the evolution of damage is based on the existence of a material property, the Fracture Toughness, defined by either the critical stress intensity factor, K_c, or critical strain energy release rate, $\mathcal{G}_c$. These two properties are equivalent. The $\mathcal{G}_c$ for the fibre-related mechanisms in each material is determined experimentally by measuring the area under the load-displacement curve during an interval of crack extension in the Compact Tension specimen (CT). The objective of this test is the study of the stable propagation of a crack tip in a brittle material in order to determine the critical strain energy release rate, $\mathcal{G}_c$. The load application is controlled by displacement, at a velocity of 0.5 mm/min. The Compact Tension specimen configuration used in the experimental campaign is shown in Figure 5.1.

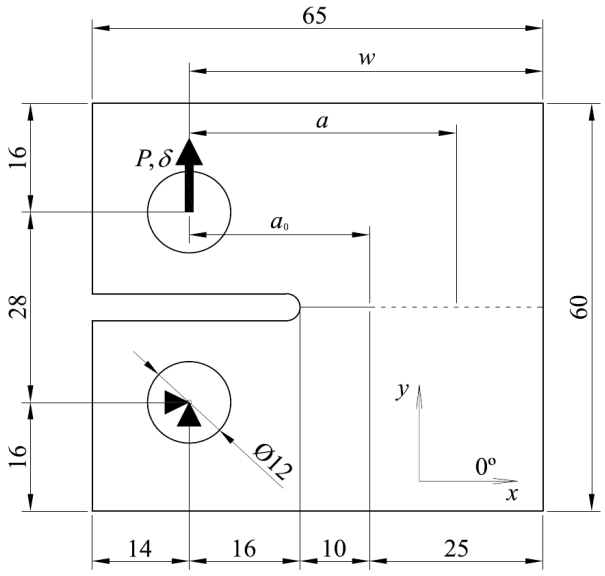

Figure 5.1: Geometric definition of the CT test configuration.

In the Compact Tension test, the fiber direction with respect to the x-direction is a test parameter. Tests on CC specimens were conducted with two different pure laminates, having the same number of plies in each orientation but a different stacking sequence with a total thickness of 4.192 mm.

- L01: $[0, 45, 90, -45]_{2s}$
- L02: $[0_2, 45_2, 90_2, -45_2]_s$

Tests on TC specimens were conducted with one pure laminated with a total thickness of 4.356 mm.

- L03: $[0, 45]_{4s}$

5.1.3 Delamination tests

Delamination is defined by the apparition of a crack-like discontinuity between the plies and its subsegment propagation during application of mechanical or thermal loads. A crack can grow in three pure modes: Mode I, Mode II, Mode III, depending on the direction of the loads with respect to the crack plane (Figure 5.2). Delamination is approached using Linear Elastic Fracture Mechanics (LEFM) which is based on the stain energy release rate, as it has been explained in section 5.1.2. Therefore, the fracture toughness for each material depends on the mode in which the crack grows.

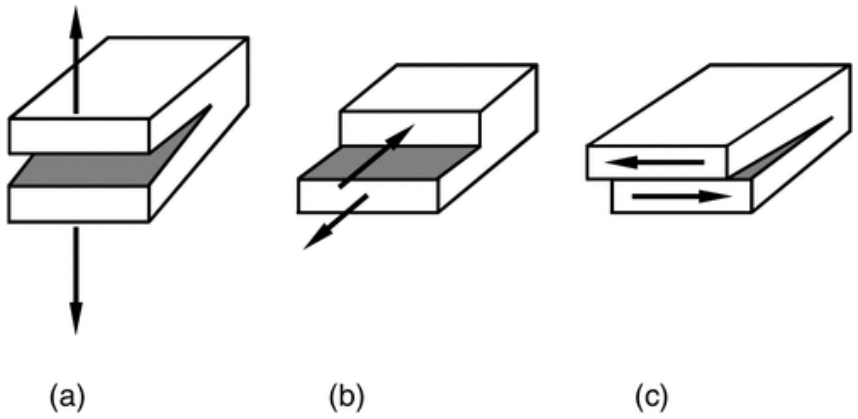

Figure 5.2: Pure modes of crack propagation. (a) Mode I. (b) Mode II. (c) Mode III.

For the characterization of the interlaminar properties of both composite materials, the following delamination tests are performed: the Double-Cantilever Beam test (DCB), the Calibrated End-Loaded Split test (C-ELS) and the Mixed-Mode Bending test (MMB), corresponding to crack propagation modes I, II, and mixed, respectively. It is assumed that the properties for mode III are equal to the ones obtained in mode II. Delamination test procedures are limited to unidirectional $[0]_n$ laminates in which a delamination propagates between the plies along the fibre direction.

The purpose of the DCB test is to determine the opening mode (mode I) interlaminar fracture toughness $\mathcal{G}_{\mathcal{I}_c}$. To measure this material property, a pre-cracked specimen is loaded continuously by peel-forces until a total propagated crack of approximately 100 mm has been achieved. The evaluation of the pure mode II fracture toughness $\mathcal{G}_{\mathcal{II}_c}$ is made by the performance of the C-ELS test. A pre-cracked specimen is loaded at the edge until crack propagation onset. The resistance to delamination growth increases as the amount of shear loading increases. How the fracture modes I and II combine to cause failure is not well established. Consequently, the purpose of the MMB test is the delamination characterization of composite materials in a mixed-mode fracture testing. In Section 6.3 the configurations of these tests will be shown in more detail in order to define the numerical models.

5.2 Material properties

Once the experimental tests described in the previous section have been performed, the properties that describe the constitutive behaviour of Unidirectional carbon-reinforced composite (CC), and fabric carbon-reinforced composite (TC) materials are presented below.

5.2.1 Material CC

The Unidirectional carbon-reinforced composite is conformed with carbon fibres G1157.6K. The fibres are embedded in an Epoxy matrix with reference “Binder 180°C Epoxy Power”. Laminates are manufactured by a Resin Transfer Moulding (RTM) process. The total thickness of the ply is 0.262 mm. The properties of a ply conformed with CC material are listed in Table 5.1. These properties were obtained through the tensile, compressive, shear and compact tension tests.

Through the delamination tests the interlaminar properties have been obtained. The properties that describe the interface behaviour are listed in Table 5.2.

CC COMPOSITE PLY PROPERTIES		
Elastic properties		
Elastic Modulus (GPa)	E_{1T}	116.735
	E_{1C}	88.025
	E_{2T}	8.303
	E_{2C}	8.303
Shear Modulus (GPa)	G_{12}	4.67
Poisson Ratio	ν_{12}	0.26
Damage Initiation		
Ultimate strengths (GPa)	X_{1T}	1.477
	X_{1C}	0.742
	X_{2T}	0.055
	X_{2C}	0.170
Fracture Toughness (kN/mm)	G_{1T}	0.105
	G_{1C}	0.024
	G_{2T}	0.000623
	G_{2C}	0.0090

Table 5.1: Composite ply properties for CC material.

CC INTERFACE PROPERTIES		
Elastic properties		
Elastic Modulus (GPa)	E	8.803
Shear Modulus (GPa)	G	4.67
Poisson Ratio	ν	0.45
Ultimate strength		
Mode I (MPa)	τ_3^o	55
Mode II (MPa)	τ_{sh}^o	93.7
Fracture toughness		
Mode I (N/mm)	$\mathcal{G}_{I_C}$	0.637
Mode II (N/mm)	$\mathcal{G}_{II_C}$	1.819
Coupling factor	η	3

Table 5.2: Adhesive interface properties for CC material.

5.2.2 Material TC

The Fabric-reinforced composite is conformed with carbon fibres G0926.6K, sizing "5131 400" and distributed in a 5 Harness-Satin configuration. Fibres are embedded in an Epoxy matrix with reference "Binder 180ºC Epoxy Power". Laminates are manufactured by a Resin Transfer Moulding (RTM) process. The total thickness of the ply is 0.363 mm. The properties of a ply conformed with TC material are listed in Table 5.3. These properties were obtained through the tensile, compressive, shear and compact tension tests.

TC COMPOSITE PLY PROPERTIES

Elastic properties		
Elastic Modulus (GPa)	E_{1T}	59.536
	E_{1C}	45.199
	E_{2T}	54.952
	E_{2C}	45.199
Shear Modulus (GPa)	G_{12}	5.1214
Poisson Ratio	ν_{12}	0.032
Damage Initiation		
Ultimate strengths (GPa)	X_{1T}	0.804
	X_{1C}	0.531
	X_{2T}	0.772
	X_{2C}	0.534
Fracture Toughness (kN/mm)	$\mathcal{G}_{1T}$	0.045
	$\mathcal{G}_{1C}$	0.017
	$\mathcal{G}_{2T}$	0.045
	$\mathcal{G}_{2C}$	0.017

Table 5.3: Composite ply properties for TC material.

Through the delamination tests the interlaminar properties have been obtained. The properties that describe the interface behaviour are listed in Table 5.4.

TC INTERFACE PROPERTIES

Elastic properties		
Elastic Modulus (GPa)	E	8.803
Shear Modulus (GPa)	G	4.67
Poisson Ratio	ν	0.45
Ultimate strength		
Mode I (MPa)	τ_3^o	55
Mode II (MPa)	τ_{sh}^o	93.7
Fracture toughness		
Mode I (N/mm)	$\mathcal{G}_{I_C}$	1.009
Mode II (N/mm)	$\mathcal{G}_{II_C}$	2.452
Coupling factor	η	1.8676

Table 5.4: Adhesive interface properties for TC material.

Chapter 6

Numerical models

In this chapter, the numerical models used to validate the model implemented in PAM-CRASH (presented in Section 3.2) are explained. The numerical models used in the project SUPERCALCULUS have been adapted from the 2012 version of PAM-CRASH to the 2016 version, the modifications made for the adapatation of the models will be explained below. In the first section of the chapter, the mesh size requirements for the performance of the following numerical test are obtained. In the second section, results of the numerical tests performed over a one-element model for different element sizes are shown. Results from these simulations are used to check the validity of constitutive laws implemented in the material for the principal directions and for the in-plane shear mechanism. In the description of the model, the procedure to describe a single ply of the composite material is explained. The third section describes the numerical models of different delamination tests (DCB, C-ELS, MMB) in a composite material in order to simulate the experimental tests used to characterize the interfase properties. In the last section of this chapter, the numerical implementation of the Low Velocity Impact test is explained through the combination of techniques to conform a whole laminate, as well as the modelling of required additional parts of the testing equipment, like the impactor.

Two different materials are used for each test: Unidirectional carbon-reinforced composite (CC) and fabric carbon-reinforced composite (TC). Therefore, in order to check the validity of the model presented in this thesis, the numerical tests are performed also using the models already implemented in PAM-CRASH libraries. Then, in Chapter 7 the results obtained with the different models will be compared with experimental results.

6.1 Mesh size requeriments

As it has been explained in Section 4.1, in an explicit finite element model the stable time increment is computed for the different elements in the mesh, regarding the element size, the material stiffness and density. The smallest value obtained for the stable time increment, considering the whole model, is the size for the time step used in the simulations.

Since the stiffness and density are material properties, that cannot be modified in an impact-related simulation, the only variable allowed to be modified, in order to ensure a minimum stable time increment in the model, is the size of the finite elements in the mesh. Since the stable time increment should not take values below 0.5 ms, it is computed for the stiffer mechanism in the materials present in this work, the material CC in the fibre direction. The material properties lead to a critical element length of $l_c \geq 4.41$ mm. In order to ensure the stable time increment for compression-related mechanisms in the whole simulaiton (i.e. where the element length is reduced due to strain), a safety margin is considered. Taking into account these considerations, a mesh refinement of $l_e = 5.00$ mm. is selected.

According to [30] a suitable representation of the cohesive zone usually results in finite elements of the order of $l_e = 0.25$ mm. This implies an elevated number of elements to be computed, specially when a whole car simulation needs to be solved. For this, Turon et al. [28] presented an engineering solution for the simulation of delamination using larger elements, by increasing the cohesive length of the interface material. This solution is achieved by reducing the strength for the onset of delamination in the material, while maintaining the corresponding fracture toughness. Therefore, a factor f_r, which scales the interface strength, is computed as proposed in [29]:

$$f_r = \frac{1}{\tau^0}\sqrt{\frac{ME\mathcal{G}_c}{N_e l_e}} \tag{6.1}$$

Then, the interfacial strengths are computed as:

$$\tau_3 = min(\tau_3^0, f_r\tau_3^0)$$

$$\tau_{sh} = min(\tau_{sh}^0, f_r\tau_{sh}^0)$$

Since the size of the elements to be used is larger than the cohesive zone lengths for the different damage mechanisms in the material, the strength reduction methodology is adopted, in order to accomplish with the recommendations in [28], where the number of elements to be embedded in the cohesive length is set between 3 and 5, in order to achieve a proper description of its behaviour.

The models developed in the project SUPERCALCULUS are used in this master thesis as reference, as well as the corresponding reductions of the interfacial strengths. Therefore, using the engineering solution, the reductions of the interfacial strengths obtained in SUPERCALCULUS are: for CC material $\tau_3 = 5.9$ MPa, $\tau_{sh} = 9.97$ MPa, for TC material $\tau_3 = 6.60$ MPa, $\tau_{sh} = 10.3$ MPa. With this values, the modified cohesive zone length is $l_{cz} = 5$ mm., fulfilling the recommendation of including between 3 and 5 elements in the cohesive zone for a mesh size equal to 1.4mm, which is the one used in the Compact Tension test performed in SUPERCALCULUS project. In the models with $l_e = 5.00$ mm., there is only one element in the cohesive length, so the reccomendation of embedding between 3 and 5 elements is not fulfilled. A further increase on the cohesive length leads to values of strength that are not large enough to ensure the structural integrity in the model (i.e. components whose geometry shows not enough space for the expanded cohesive zone to be fully developed and propagated are untied at low force levels, affecting the overall behaviour of the structure). Therefore, in order to obtain a good correlation on the tests with an element size of 5 mm., a manual adjustment was made using values of τ_{sh} between 5 MPa and 15 MPa. Finally, an optimal value of $\tau_{sh} = 12$ MPa was obtained, which is the one used in this master thesis.

To sum up, two element sizes are then considered for the simulations of the different tests in this work: $l_e = 5.00$ mm., in order to accomplish with the stable time increment requeriments, and $l_e = 1.40$ mm., which is maximum permissible size for the crack width in the precrack of the compact tension tests. In this project the compact tension tests will not be performed, due to numerical inestabilities shown by the solver for this kind of simulation. Therefore, the element size 1.4 mm. is going to be used to check the mesh independency of the implemented model and the mesh influence in the material used to simulate the interface between plies in delamination tests.

6.2 One element tests

In this section the numerical models used to simulate one element tests are presented. These models are used to check the laws implemented in the material. Classical theories originally developed for isotropic single-layer structures, such as Kirchhoff and Mindlin-Reissner plate theories, have been extended for modelling of composites. These theories are based on plane stress assumptions. In this approach, the plies in the composite are homogenized through the thickness by means of laminate theory, and are therefore referred to as an equivalent single layer model.

In this master thesis, each element represents a ply of the composite material. Individual plies and sub-laminates are modelled with 4-node shell elements (Figure 6.1). The shell material labelled as 131 in Pam-Crash is used for modelling plies due to its compatibility with most of the constitutive models for composite plies. This material corresponds to multilayered and multi-material shell models in which the layers can consist of material modeled as elastic damaging fiber-matrix composite. An example of a multilayered shell can be observed in 6.2. Each specified ply corresponds to one integration point across the thickness of the shell, located at the center of the ply.

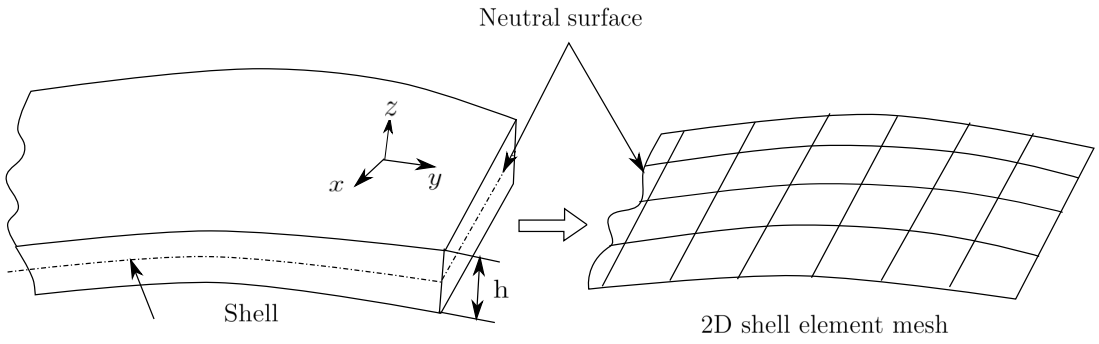

Figure 6.1: 4-noded shell mesh.

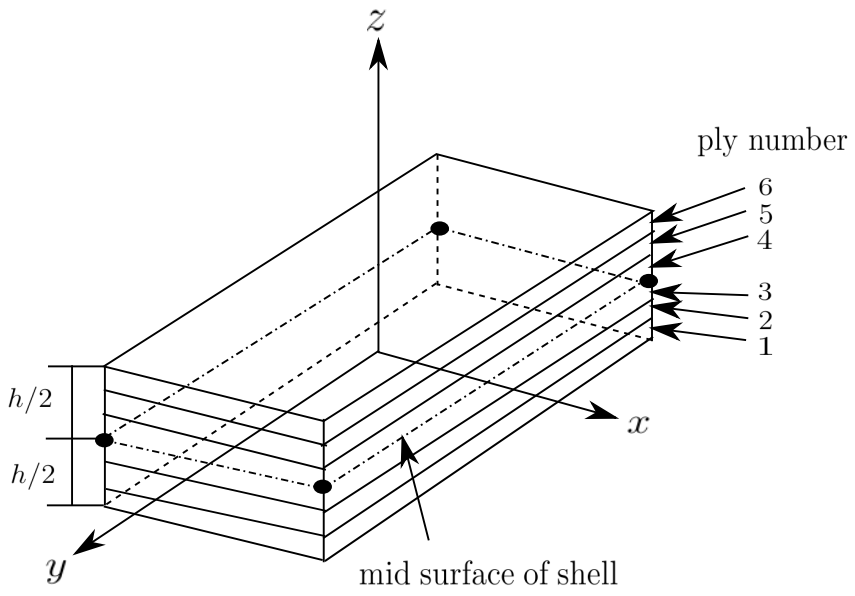

Figure 6.2: Multilayered shell with 6 plies.

Ply properties are selected from the composite ply. Therefore, in order to define the composite laminae properties according to the existing models in PAM-CRASH, two types of plies are chosen from the libraries of PAM-CRASH. Ply type 1 has been selected for material CC. This ply definition is based on a paper by P. Ladevèze and E. Ledantec and modified to include transverse shear by A. Hurez. Whereas, for material TC ply type 7 has been selected, which corresponds to the adaptation of the Ladevèze model for fabric-reinforced composites. The form in which the Ladevèze's model is implemented shows some limitations to reproduce the constitutive law for certain combinations of ultimate strength (X_M) and fracture toughness ($\mathcal{G}_M$) in function with the size of the element. Meaning that for some element sizes the materials cannot be modelled using their properties. Besides, in the ply model type 1 damage variables for the fibre-related mechanisms are expressed as a function of the strains, and in the adaptation of the Ladevèze model for textile plies damages variables are expressed as a function of the energy release rates, values that are computed from the material properties. Therefore, the material properties used for the definition of plies type 1 and 7 are obtained using the numerical tools developed in the project SUPERCALCULUS. The purpose of these numerical tools is to ensure a correct energy dissipation for each damage mechanism when the material properties are not compatible with the mesh refinement.

The user-subroutine implemented in PAM-CRASH corresponds to the ply model type 10. As it has been explained, Bažant's Crack Band Model has been implemented in this model, therefore the material properties are independent of the element size and the materials can be modelled using their properties. Moreover, it can be used both for unidirectional fibre-reinforced composites and for fabric-reinforced composites. Thus, only one material property card is defined for each material. Taking into account that direction 1 is aligned with the fibres with the strongest properties and direction 2 is aligned with the matrix or the warp tows, for UD or fabric-reinforced composites, respectively, the inputs needed to define the user ply model type 10 card are:

- E_{1T},E_{1C} = Longitudinal Young's Modulus.
- E_{2T},E_{2C} = Transverse Young's Modulus.
- G_{12} = Shear modulus in 1,2 plane.
- G_{23} = Shear modulus in 2,3 plane.
- G_{13} = Shear modulus in 1,3 plane.
- ρ = Mass density of ply material.
- ν_{12} = Poisson ratio in 1,2 plane.
- ν_{21} = Poisson ratio in 2,1 plane.
- $X_{1T}, X_{2T}, X_{1C}, X_{2C}$ = Ultimate strength.
- $H_{1T}, H_{2T}, H_{1C}, H_{2C}$ = Slope of the first region of the cohesive law.
- $\mathcal{G}_{1T}, \mathcal{G}_{2T}, \mathcal{G}_{1C}, \mathcal{G}_{2C}$ = Fracture energy.
- $f_{X_{1T}}, f_{X_{2T}}, f_{X_{1C}}, f_{X_{2C}}$ = Pull-out stress.
- $\eta_{1T}, \eta_{2T}, \eta_{1S}, \eta_{2S}$ = Coupling factor.
- S_{LP} = Shear plastic initiation.
- ς_E, ς_E^T,ς_L = Shear plastic adjustement factors.

In the models of ply types 1 and 7 of Pam-Crash, the values of the coupling factors, the pull-out stresses and the slopes of the first stages of the cohesive laws can not be introduced, so they are out of the scope of the Supercalculus project. The coupling factors are included in the model to give more flexibility to the failure envelopes, but in this project they have not been correlated so they are set to 0. On the other hand, the pull-out stresses and the slopes have been obtained in some tests carried out in Abaqus in [1, 23]. The pull-out mechanism begins around values of forces between 150 kN and 250 kN, and the slopes of the first stages of the cohesive laws are defined by means of the total fracture toughness minus the toughness related to the pull-out mechanism. These values have been used in this master thesis in order to be able to compare the results obtained in Pam-Crash with those obtained with the same constitutive model in Abaqus.

For one element tests, each failure mechanism is simulated by charging the element uniaxially in different cases. In Figure 6.3 each case is represented. The element sizes used for one element test simulations are 5 mm and 1.4 mm.

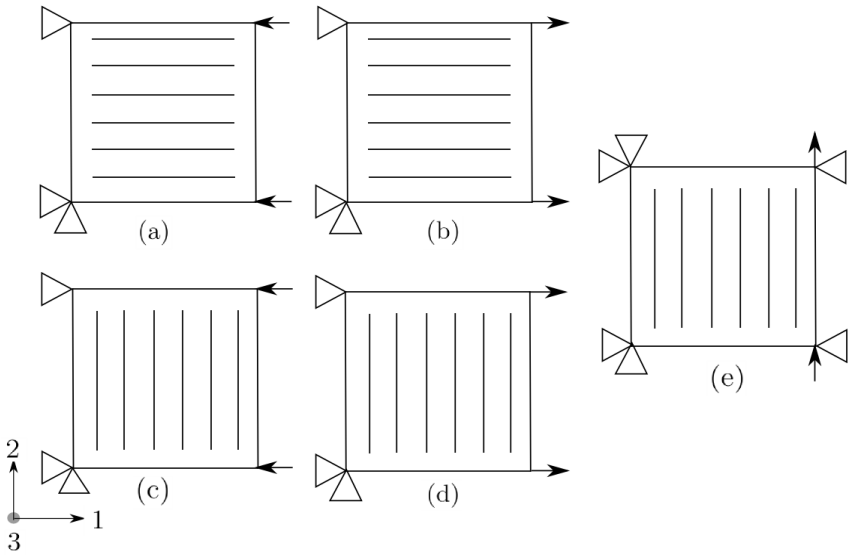

Figure 6.3: Setup for one element tests. (a) Compressive load in longitudinal direction. (b) Tensile load in longitudinal direction. (c) Compressive load in transverse direction. (d) Tensile load in transverse direction. (e) Shear loading.

6.3 Delamination

In this section, delamination tests are simulated numerically in order to check the validity of the constitutive laws of the model implemented in ply type 10. Three modes of delamination are tested, the pure modes I and II, and the mixed mode with a mixed mode ratio B equal to 0.5, called DCB, C-ELS and MMB, respectively. The mixed mode ratio parameter (B) describes the perentage of mode II present in the crack propagation event, defined as:

$$B = \frac{\mathcal{G}_{\mathcal{II}}}{\mathcal{G}_{\mathcal{I}} + \mathcal{G}_{\mathcal{II}}} \tag{6.2}$$

These tests are performed over pre-cracked specimens with the materials CC and TC. The configuration of the specimen for each material is:

- Material CC: 12 plies oriented at 0º. Total thickness = 3.144 mm.
- Material TC: 8 plies oriented at 0º. Total thickness = 2.904 mm.

The scheme of the generic specimen used for the delamination tests is shown in Figure 6.4. The values of the parameters defining the geometry will be detailed for each test.

Figure 6.4: Geometric definition of the generic specimen.

In order to simulate the delamination mechanism, the behaviour of the interface between the central plies of the laminate must be simulated. Numerical models are performed over two plies linked by "tie" elements. That is, the whole laminate is splitted into two sub-laminates, i.e. h_a value corresponds to one half of the total thickness. Each sub-laminate is modelled using one stacked shell element in the thickness direction. Tie elements are included in Pam-Crash libraries. The material labelled as 303 is chosen to define the mechanical properties used in the two tied interfaces. Since it is the one that simulates adhesive unions, is the best option to simulate the interface between plies. For

the simulation of the degradation of the tie element, IDELA parameter is set to 1, which corresponds to the delamination model Benzeggagh-Kenanee. This formulation takes into account the coupling between delamination mode behaviours. Moreover, the rotational degrees of freedom of the shell nodes are not tied, this is chosen through the parameter I3DOF which is set to 1.

According to the interlaminar properties presented in Tables 5.2 and 5.4, the following parameters are defined in the material 303 in Pam-Crash:

- SIGMApr (τ_3) and GAMMApr (τ_{sh}) define the values of the normal stress and shear stress propagation of delamination, respectively, corresponding to the reduced interfacial strengths obtained in Section 6.1.

- SIGMAst (τ_3) and GAMMAst (τ_{sh}), are the values of the normal stress and shear stress for delamination initiation, which correspond to a shift of the maximum allowed stress to start the delamination process. Due to the application of the strength reduction, this capability is not used.

- ETA (η) corresponds to the coupling factor.

Due to the adaptation of the numerical models to the 2016 version, the influence of some parameters defined in material 303 have changed. One of them is the parameter IDEABEN which updates the tied normal. There are five options availables but only two of them are recommended for shells and explicit analysis. IDEABEN = 0 is based on master segment normal while IDEABEN = 4 is based on mean roation Master/slave. After some studies of the influence of this parameter, it has been concluded that for delamination tests the best option is IDEABEN = 4, while for the low velocity impact tests IDEABEN = 0 offers more accurate results.

In addition, a contact algorithm is included in order to avoid interpenetration between the different plies when a tie element is eliminated. Contact interfaces model the interaction between structures and parts of structures that are not permanently connected by standard finite element connectivity conditions. There are several types of contact interfaces available in Pam-Crash. The contact labelled as “36”, which corresponds to

a "Self-Impacting Node-to-segment with edge treatment", is chosen. It requires the definition of only one of the surfaces that might get into contact with in the simulation. The contact thickness is fixed to the thickness of the ply.

The ply and interface material properties are listed in Chapter 5. The element sizes used for the simulations are 5 mm and 1.4 mm.

6.3.1 Mode I: DCB Tests

For the numerical model of Double-Cantilever Beam (DCB) test, the values of the parameters that define the geometry of the specimen (Figure 6.4) are the following:

- Length of the specimen ($2L$): 250 mm.
- Width of the specimen (b): 25 mm.
- Initial crack length (a_0): 25 mm.

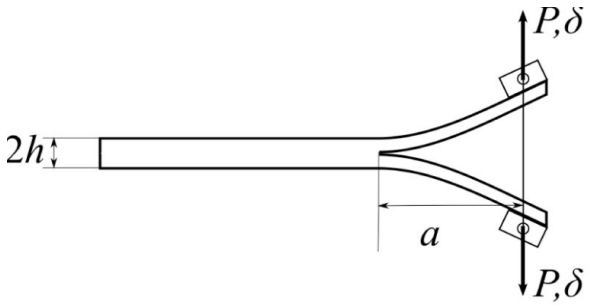

Figure 6.5: Double-Cantilever Beam (DCB) test configuration.

The boundary conditions for the numerical simulation consist of two imposed displacements in opposite z-directions at the tip of the specimen ($x = 2L$) and all nodes clamped in $x = 0$. In Figure 6.5 a scheme of the model is shown with the corresponding boundary conditions responsible for effecting a mode I stress field at the interface. The corresponding model in Pam-Crash is shown in Figure 6.6(a). In addition, in order to have a better

understanding of the behaviour of the test, in Figure 6.6(b) is shown the model at $t = 10$ ms.

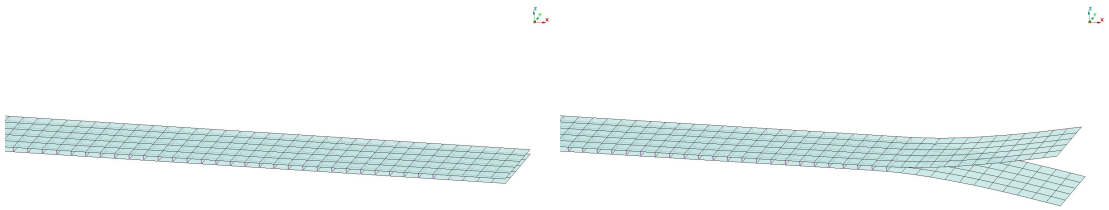

(a) Mesh for DCB simulations. (b) DCB model at t = 10 ms.

Figure 6.6: Numerical model for Double-Cantilever Beam (DCB) tests.

6.3.2 Mode II: C-ELS Tests

For the numerical model of Calibrated End-Loaded Split (C-ELS) test, the values of the parameters that define the geometry of the specimen (Figure 6.4) are the following:

- Length of the specimen ($2L$): 105 mm.
- Width of the specimen (b): 25 mm.
- Initial crack length (a_0): 57 mm.

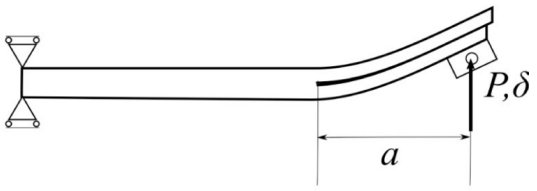

Figure 6.7: Calibrated End-Loaded Split (C-ELS) test configuration.

The boundary conditions for the numerical simulation consist of one imposed displacement in the z-direction at the tip of the specimen ($x = 2L$) and all nodes clamped in $x = 0$. In Figure 6.7 a scheme of the model is shown with the corresponding boundary conditions responsible for effecting a mode II stress field at the interface. The corresponding model in PAM-CRASH is shown in Figure 6.8 (a). In addition, in order to have a better understanding of the behaviour of the test, in Figure 6.8(b) is shown the model at $t = 60$ ms.

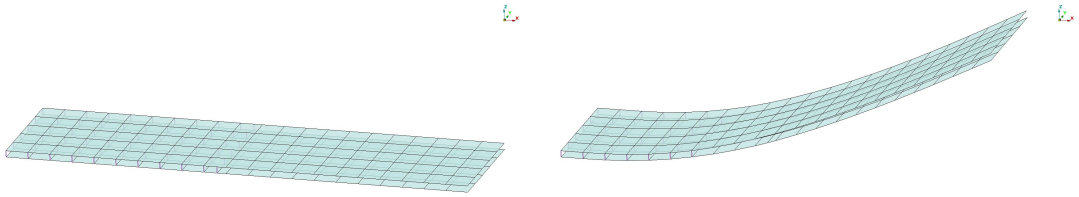

(a) Mesh for C-ELS simulations. (b) C-ELS model at time $t = 60$ ms.

Figure 6.8: Numerical model for Calibrated End-Loaded Split (C-ELS) tests.

6.3.3 Mixed Mode: MMB Tests

For the numerical model of Mixed-Mode Bending test, the values of the parameters that define the geometry of the specimen (Figure 6.4) are the following:

- Length of the specimen ($2L$): 100 mm.
- Width of the specimen (b): 25 mm.
- Initial crack length (a_0): 25 mm.

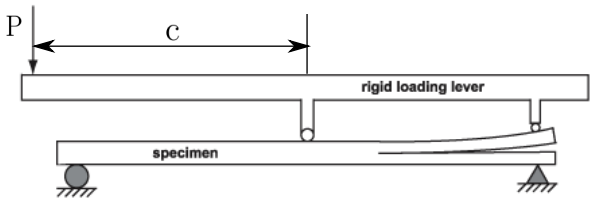

Figure 6.9: Mixed-Mode Bending (MMB) test configuration.

The boundary conditions for the numerical simulation consist of one imposed displacement in the z-direction at the centre of the loading arm, nodes at $x = 0$ with translation fixed in y and z directions and rotation fixed in z-direction, nodes at $x = 100$ with translation fixed in x,y,z-directions and rotation in z-direction. In Figure 6.9 it is shown a scheme of the model with the corresponding boundary conditions responsible for effecting a mixed-mode stress field at the interface. The distace c between the point of load application and the midpoint of the specimen determines the mode mixity. That is, pure mode I corresponds to an infinite-length loading arm while a pure mode II corresponds to $c = 0$. The corresponding model in PAM-CRASH is shown in Figure 6.10(a). In addition, in order to have a better understanding of the behaviour of the test, in Figure 6.10(b) is shown the model at $t = 200$ ms.

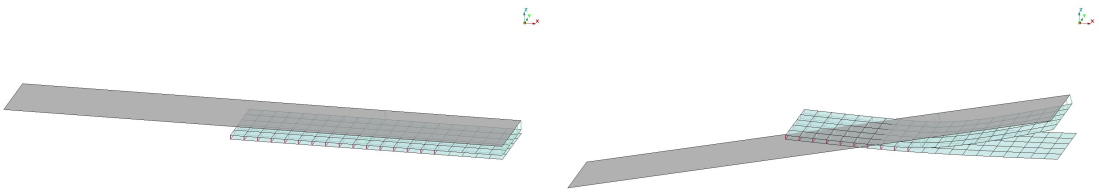

(a) Mesh for MMB simulations.

(b) MMB model at $t = 200$ ms.

Figure 6.10: Numerical model for Mixed-Mode Bending (MMB) test.

6.4 Low Velocity Impact test

Low Velocity Impact simulations (LVI) are used to determine the damage resistance of multi-directionl polymer matrix composite laminated plates subjected to a drop-weight impact event. Interlaminar stresses occur in the boundary layer of laminates under transverse loading. The polymeric matrix in the material allocates the energy inside it and makes it capable of absorbing impact energy. The low velocity impact test does not produce perforation, but creates delaminations between the layers with barely visible damage on surfaces, and eventually a small amount of fibre-damage in the impact point. There are a few parameters that affect failure modes in composite materials due to low velocity impact loading conditions: type of fibre, resin, lay-up, specimen thickness, velocity and type of projectile. In Figure 6.11 is it shown a representation of the LVI test configuration.

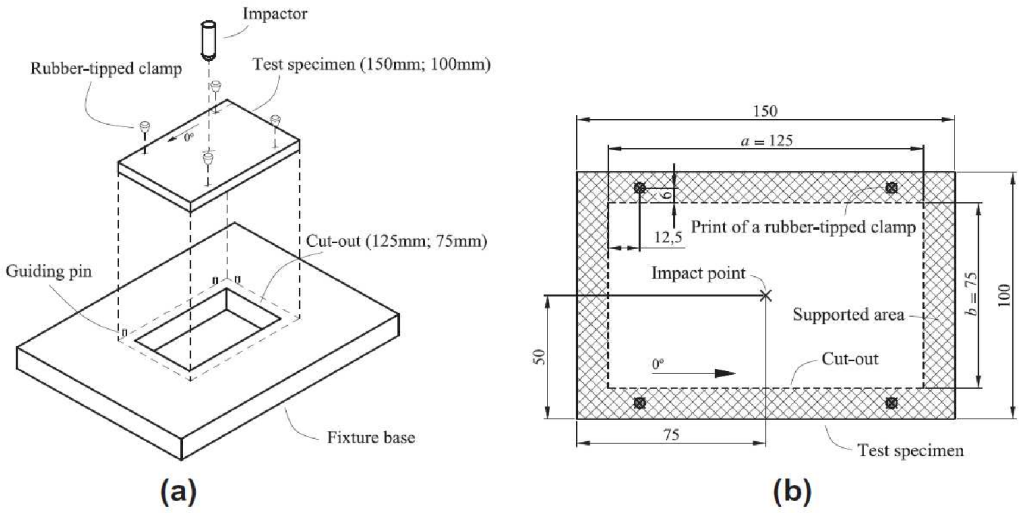

Figure 6.11: Geometric definition of the LVI test configuration. (a) Impact support fixture. (b) Detail of the support area and clamping points of the specimen.

Plies and laminates are modelled using the same procedures used for the previous models. Therefore, for the numerical model of the specimen, a rectangular shell of composite material is used. The reduced interfacial strengths defined in delamination tests can not be used in LVI models, since the equations used to compute the engineering solution do not work for radial damage growth. For LVI tests, the interfacial strengths obtained in the experimental tests in Tables 5.2 and 5.4 are used directly in the material 303.

Some parts of the equipment must be modelled as rigid bodies in the numerical simulation. These parts are: the impactor, the base shell and fixture rubber. The impactor is the part where the initial velocity is applied, the base shell is the part in which the specimen is supported and fixture rubber are four parts which fix the specimen to the base shell. A null material labelled as 100 is applied to these parts. In order to make the parts of the equipment undeformable, a rigid body type 1 constraint is applied. In addition, new contact definitions are added in order to define the interactions between the new parts and the specimen in the model. Contact labelled as "34" is used for the interactions between the specimen and the impactor, the base shell and rubber fixtures, which corresponds to a "Non-symmetric node-to-segment with edge treatment". Due to a refinement in the mesh of the specimen and some of the rigid body parts, it is necessary to add a new contact definition in order to avoid a bad description of the contact interaction. Thus, contact labelled as "43" is added to the interactions between the specimen and the impactor, and the specimen and the base shell.

As it has been explained in the previous section, for LVI simulations the parameter IDEABEN is set to 0. The final numerical model of the LVI test is shown in Figure 6.12. The element size used for the specimen is 5 mm.

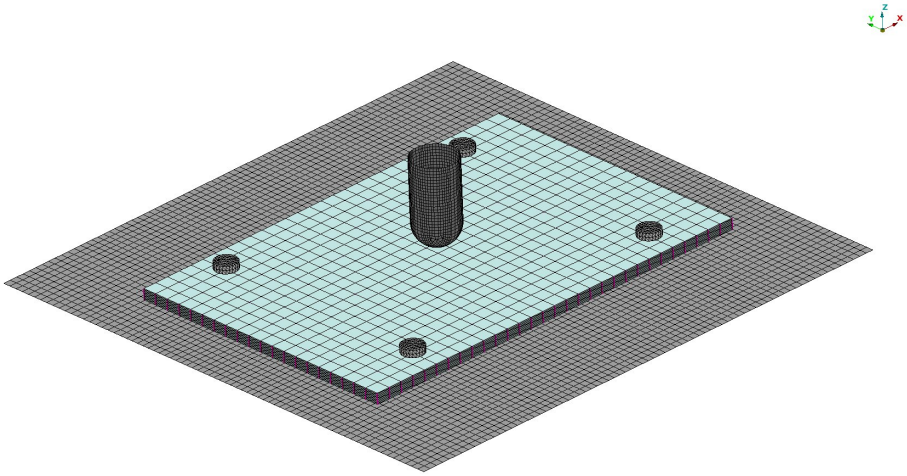

Figure 6.12: Mesh LVI simulations.

Chapter 7

Validation and industrial application

In this chapter, the numerical results for the models presented in Chapter 6 are presented for each material. Tests over one element are performed in order to validate and demonstrate the stress-strain behaviour for a single layered composite specimen in the different damage mechanisms considered in the model. Once the constitutive laws are validated for each element size, the results for the delamination tests used to characterize the interfase properties are presented. Finally, the numerical results for the Low Velocity Impact (LVI) test are shown. In difference with the rest of the tests, which where used to characterize some mechanical properties, LVI tests are used to cause a combined state of damage in the material. In this case, the performance of large specimens conformed with composite materials is tested.

7.1 Material CC

7.1.1 One element tests

In this section, the results for the numerical simulations over one element models for each load case presented in Figure 6.3 are shown. For this, the stress-strain relation and the dissipated energy per area for element sizes of 5 mm and 1.4mm are presented for the ply models type 1 and 10. Once the behaviour of each damage mechanism of the model presented in Chapter 3 is validated, the ply properties used to define both ply models will be used in the posterior models for the CC material.

In Figure 7.1 the comparisson of the stress-strain relation between the ply model type 1, model already implemented in PAM-CRASH libraries, and ply model type 10, model implemented as a user-subroutine in this master thesis, can be observed. Tensile and compressive loads correspond to red and blue lines, respectively, in the longitudinal and transverse direction. On the other hand, the dashed line corresponds to the ply model type 1, while the continuous line represents the results for the ply model type 10 (user-subroutine). The stress-strain responses match with the expected damage mechanisms defined in Chapter 3 and ultimate strengths obtained in the experimental tests. But, since the ply model type 1 does not consider a damage mechanism for the matrix under compression loads, the non-linearity observe is defined by the plastic law.

Furthermore, in Figure 7.2 the dissipated energy per area is represented. It can be seen how for both ply models the obtained energy is the same, corresponding to the fracture toughness in each direction for each damage mechanism: $\mathcal{G}_{1T} = 0.105$ kN/mm, $\mathcal{G}_{1C} = 0.024$ kN/mm, which can be observed in Figure 7.2 (a), red and blue line, respectively. $\mathcal{G}_{2T} = 6 \times 10^{-4}$ kN/mm, $\mathcal{G}_{2C} = 0.009$ kN/mm, presented in Figure 7.2 (b), red and blue line, respectively.

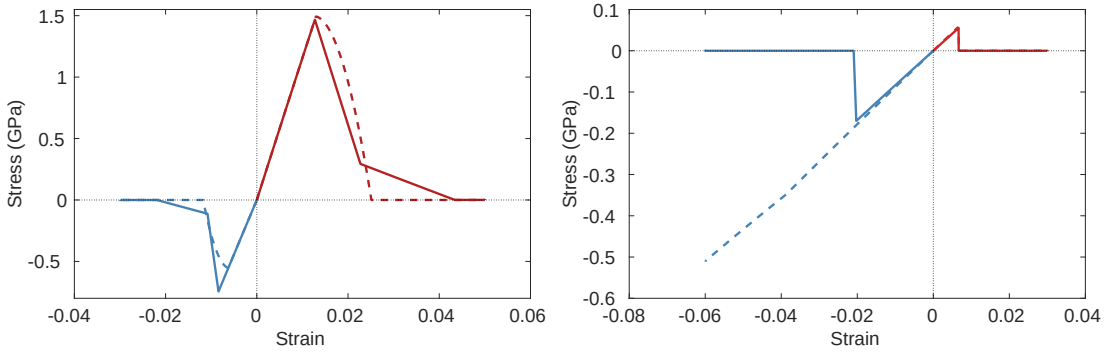

(a) Longitudinal direction (b) Transverse direction

Figure 7.1: Stress-strain curve for one element test for the material CC with an element size of 5 mm.

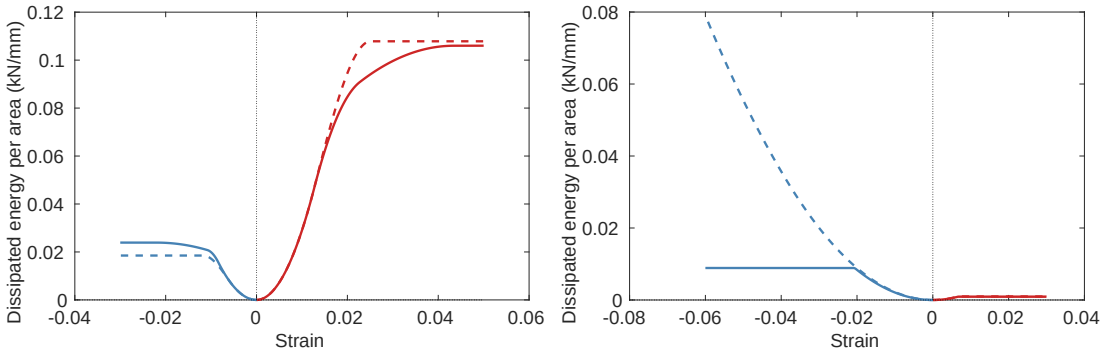

(a) Longitudinal direction (b) Transverse direction

Figure 7.2: Dissipated energy per area for one element test for the material CC with an element size of 5 mm.

The shear response is represented in Figure 7.3. For ply model type 1 a damage mechanism is considered in the shear direction, as can be observed in 7.3, while ply model type 10 does not consider a damage mechanism in the shear direction but an isotropic hardening plastic deformation.

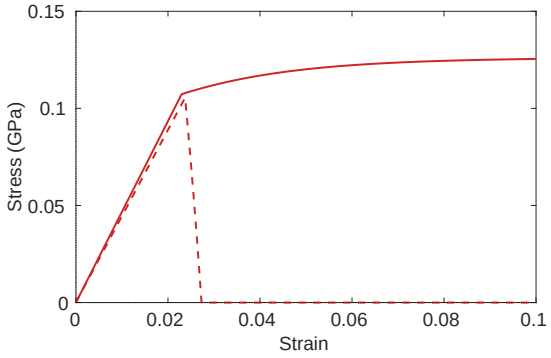

Figure 7.3: Stress-strain curve for a shear loaded element for the material CC with an element size of 5 mm.

As it has been explained in the previous chapter, the constitutive equations are also validated for an element size of 1.4 mm (Figures 7.4, 7.5 and 7.6)

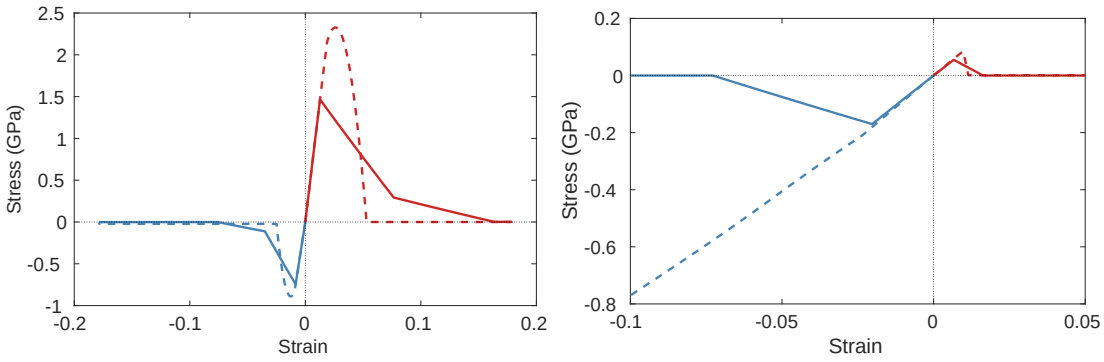

(a) Longitudinal direction (b) Transverse direction

Figure 7.4: Stress-strain curve for one element test for the material CC with an element size of 1.4 mm.

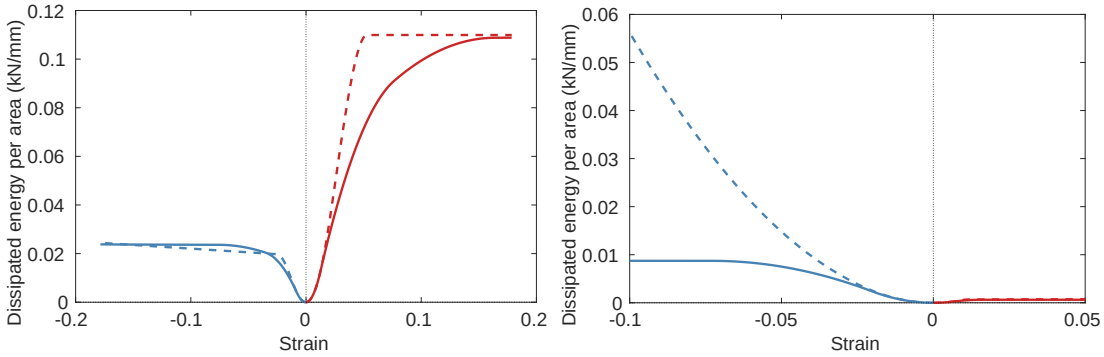

(a) Longitudinal direction (b) Transverse direction

Figure 7.5: Dissipated energy per area for one element test for the material CC with an element size of 1.4 mm.

Comparing the fibre, matrix and shear responses, it can be observed that for each damage mechanism, the ultimate strength and dissipated energy per area are equal for both element sizes in ply type 10. This is obtained by means of the application of the same material definition, demonstrating the mesh independency of the model implemented in this master thesis. To achieve an equivalent toughness level in ply type 1 for both element sizes, two different material cards must be defined. Another limitation observed in ply type 1 is that for the definition of the finest elements with the proper value of fracture toughness, the ultimate strength must be increased. This causes that the definition of

a wide combination of ultimate strength and toughness in the composite material is not allowed. This limitation is overriden in the presented model, where a linear evolution of $\sigma(\varepsilon)$ is implemented, instead of the linear evolution of $d(\varepsilon)$ implemented in ply type 1.

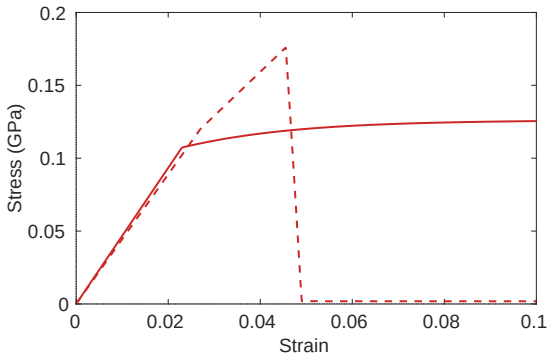

Figure 7.6: Stress-strain curve for a shear loaded element for the material CC with an element size of 1.4 mm.

7.1.2 Delamination

In this section, the results for the delamination tests of the unidirectional reinforced composite (CC) are presented. In the first place, the numerical results for the pure modes I and II, DCB and C-ELS, respectively, are shown. Once the properties of the interface have been adjusted for these modes, a mixed mode of delamination (MMB) is tested.
For this, the force-displacement curves for element sizes of 5 mm and 1.4 mm are presented for the ply models type 1 and 10, in order to study the mesh influence in the material 303. In addition, the results obtained in the SUPERCALCULUS project using the ply model type 1 with the 2012 version of PAM-CRASH are presented in order to observe the differences between versions and how they have been overcome.

7.1.2.1 Mode I: DCB Tests

Numerical simulations of DCB tests, previously defined in Section 6.3, for the material CC and element sizes of 5 mm. and 1.4 mm. are performed. The properties of the ply are the ones used in the one element tests, while the interlaminar properties are chosen according to Table 5.2 and the reduced value of the interfacial strength $\tau_3^0 = 5.9$ MPa obtained in Chapter 6.

In Figures 7.7 and 7.8 the results obtained in the simulations for an element size of 5 mm and 1.4 mm, respectively, are shown. It can be observed how numerical results lose precision in the peak where the delamination should be onset, due to the strength reduction applied to compensate the coarse mesh. After the beginning of delamination, the progression matches with the experimental and analytical results. Moreover, on the model with an element size of 1.4 mm. a better accuracy that the one with an element size of 5 mm. is obtained.

Regarding the differences between versions, the loss of precision is more pronounced in the 2016 version. However, this problem has been almost overcome using the parameter IDEABEN equal to 4 instead of 0, as it has been explained in Section 6.3. This parameter is related to how the normal to the tie element is updated. The accuracy in the peak on the force-displacement curve gets worse in the new version of PAM-CRASH without the new configuration of the parameter IDEABEN.

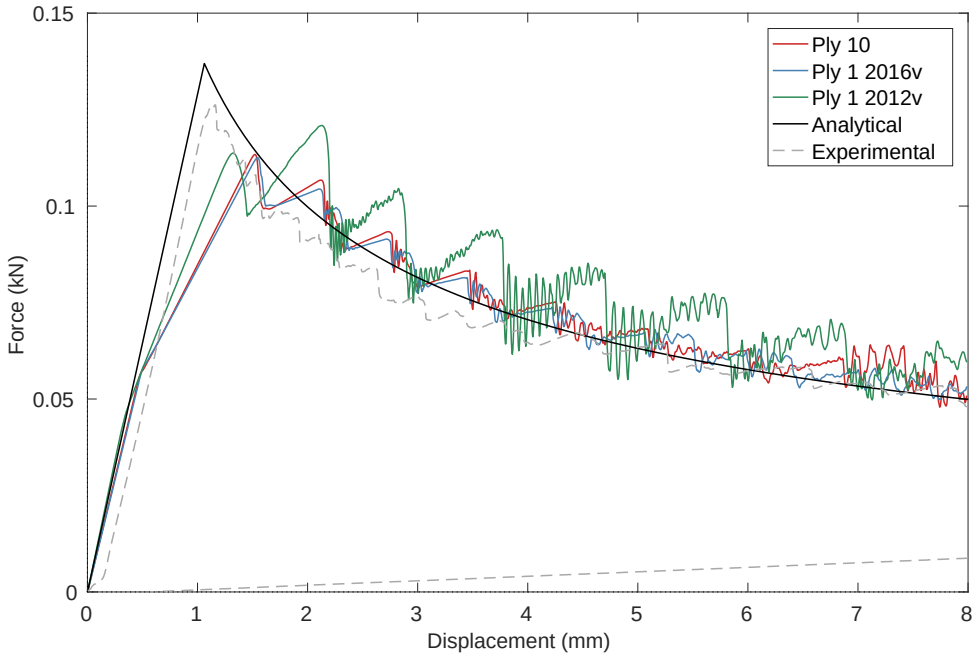

Figure 7.7: DCB results for the material CC with an element size of 5 mm.

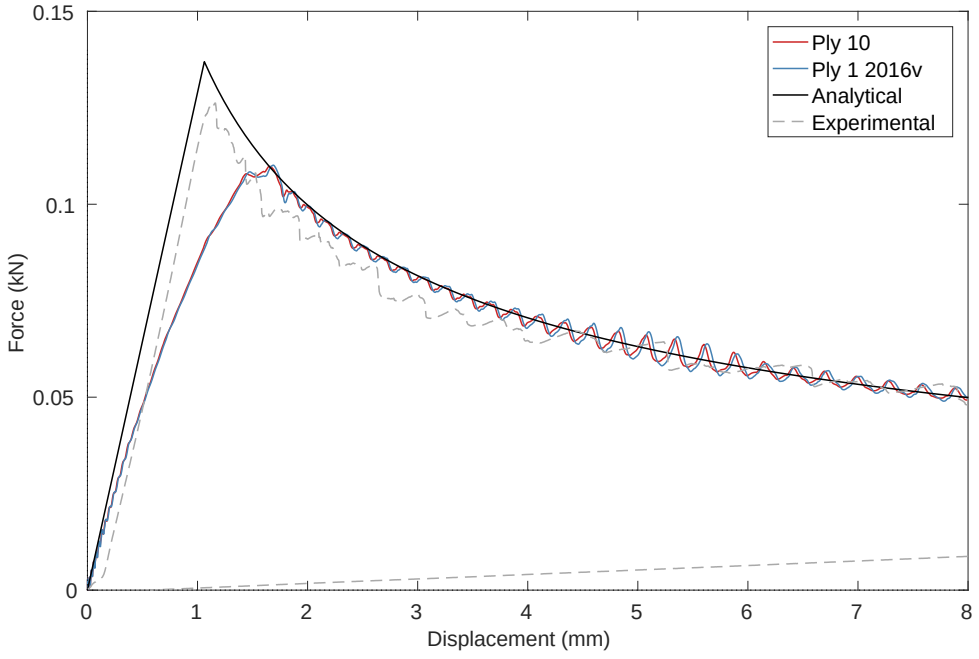

Figure 7.8: DCB results for the material CC with an element size of 1.4 mm.

.

7.1.2.2 Mode II: C-ELS Tests

Numerical simulations of C-ELS tests, previously defined in Section 6.3, for the material CC and element sizes of 5 mm. and 1.4 mm. are performed. The properties of the ply are the ones used in the one element tests, while the interlaminar properties are chosen according to the Table 5.2 and the reduced value of the interfacial strength $\tau_{sh}^{0} = 12$ MPa presented in Chapter 6.

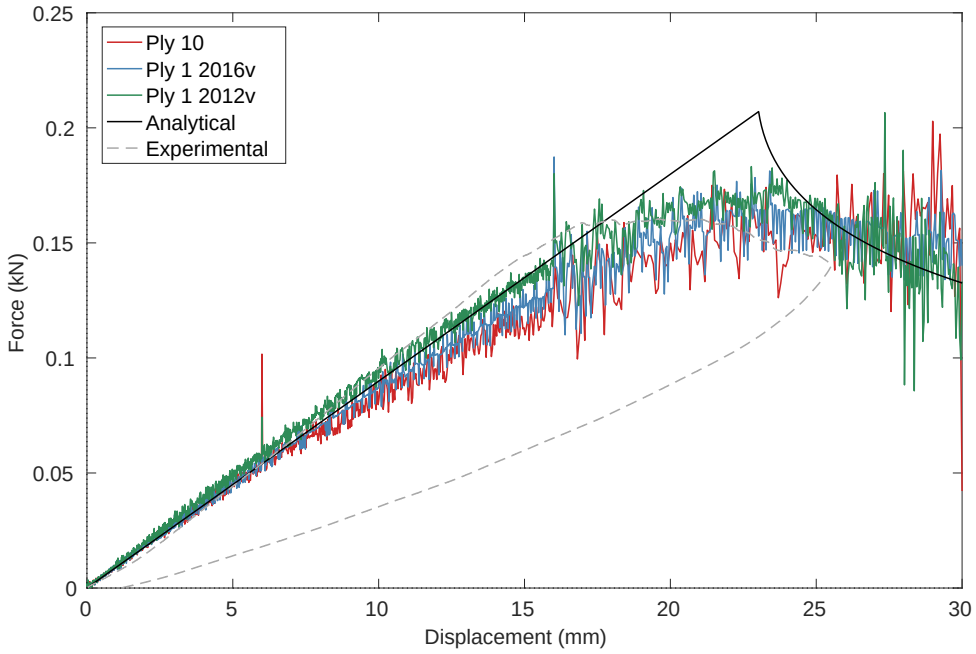

Figure 7.9: C-ELS results for the material CC with an element size of 5 mm.

In Figures 7.9 and 7.10 the results obtained in the simulations for an element size of 5 mm and 1.4 mm, respectively, are shown. As it was observed in the DCB tests, numerical results of C-ELS test lose precision in the peak where the delamination should be onset, due to the strength reduction. After the onset of delamination (i.e. in the propagation stage), the experimental and analytical results show a good level of correlation with the numerical ones. Moreover, a more oscillating response is observed, due to the test configuration: a large part of the specimen is untied at the onset of the test. This, in combination with the load application method, causes that in the numerical models, the force must be transmitted by the contact definition between the specimen arms, as a frictional sliding

force. This becomes in this oscillating response. This effect is specially notorious in the later stages of the analysis (when the crack has been already propagated) and in the models with a finer mesh. In both cases, the behaviour of a larger number of nodes becomes influenced by the frictional sliding contact definition, increasing the oscillation amplitude.

Regarding the differences between constitutive models, the ply type 10 shows oscillations of larger amplitude than the ply type one. This can be explained by two factors: a more accurated definition of the stable time increment computation is applied on ply type 1, which is not available for ply type 10. The second factor affecting the oscillating level in the results is the management of the transverse shear effects in the model, in which the definition of ply type 1 is not available for ply type 10.

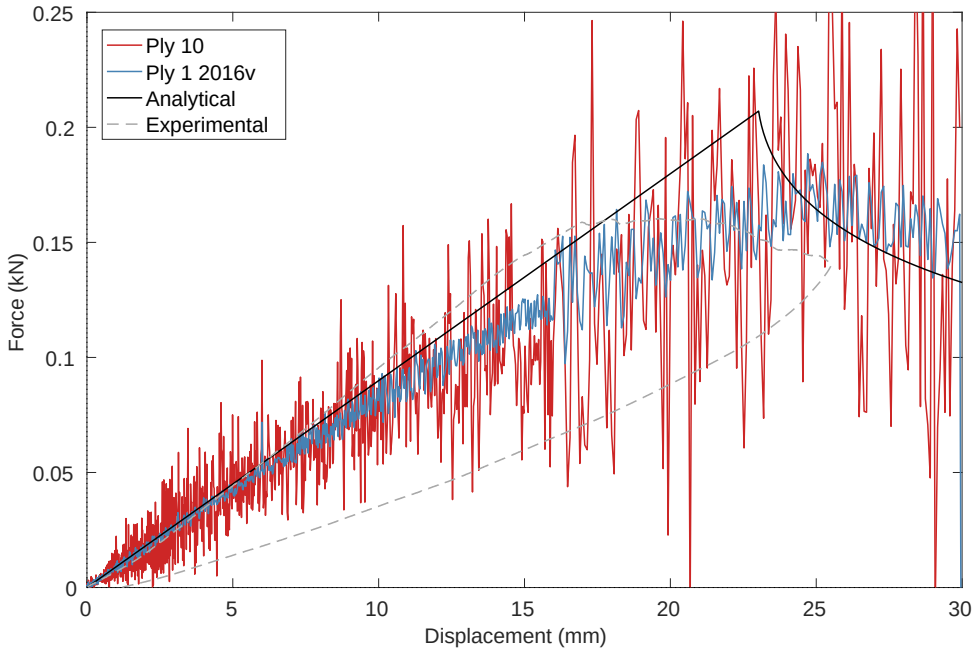

Figure 7.10: C-ELS results for the material CC with an element size of 1.4 mm.

7.1.2.3 Mixed Mode: MMB Tests

Numerical simulations of MMB tests with a mixed mode of 50%, previously defined in Section 6.3, for CC material and element sizes of 5 mm. and 1.4 mm., are performed. The properties of the ply are the ones used in the one element tests, while the interlaminar properties are chosen according to the values used in the DCB and C-ELS tests.

Mixed mode of delamination gives a worse description of the force-displacement curve. As can be observed in Figure 7.11 for 2012 version of PAM-CRASH the curve is overestimated, while for the new version for both ply models a better correlation of the progression is obtained after the onset of delamination but a loss of precision in the peak. In Figure 7.12, MMB simulations with a mesh of 1.4 mm is shown. On the model with an element size of 1.4 mm., a better accuracy is obtained before the onset of delamination. As it happened in C-ELS tests, an oscillating response is obtained, but in this case in a smaller amplitude, since the tensile component of the mixed mode reduces the influence of the frictional sliding force.

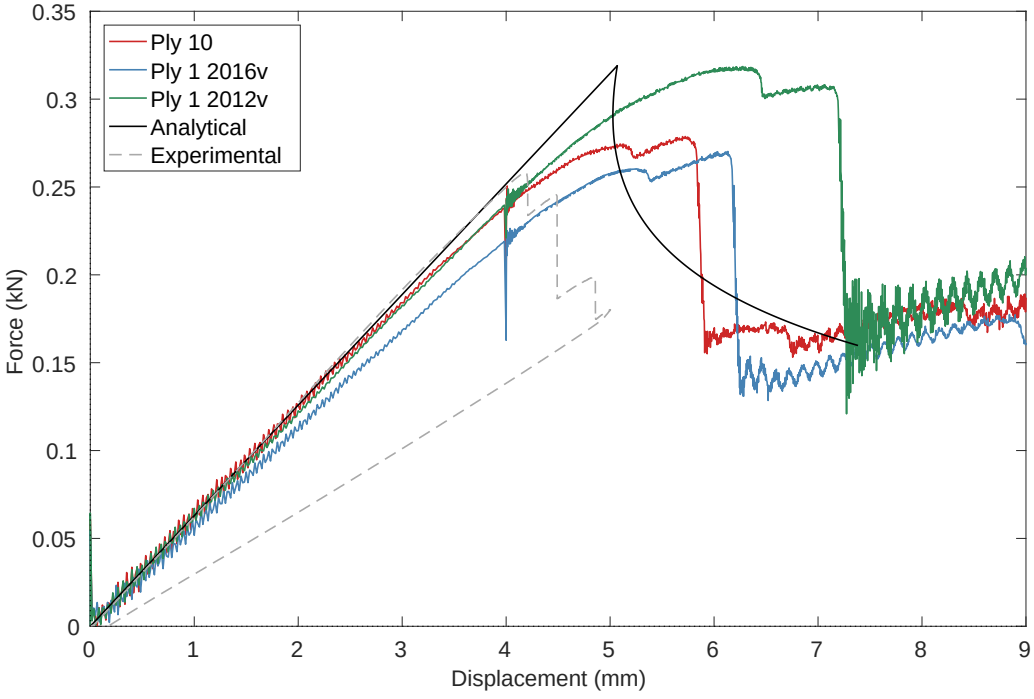

Figure 7.11: MMB results for the material CC with mixed-mode ratio 50% with an element size of 5 mm.

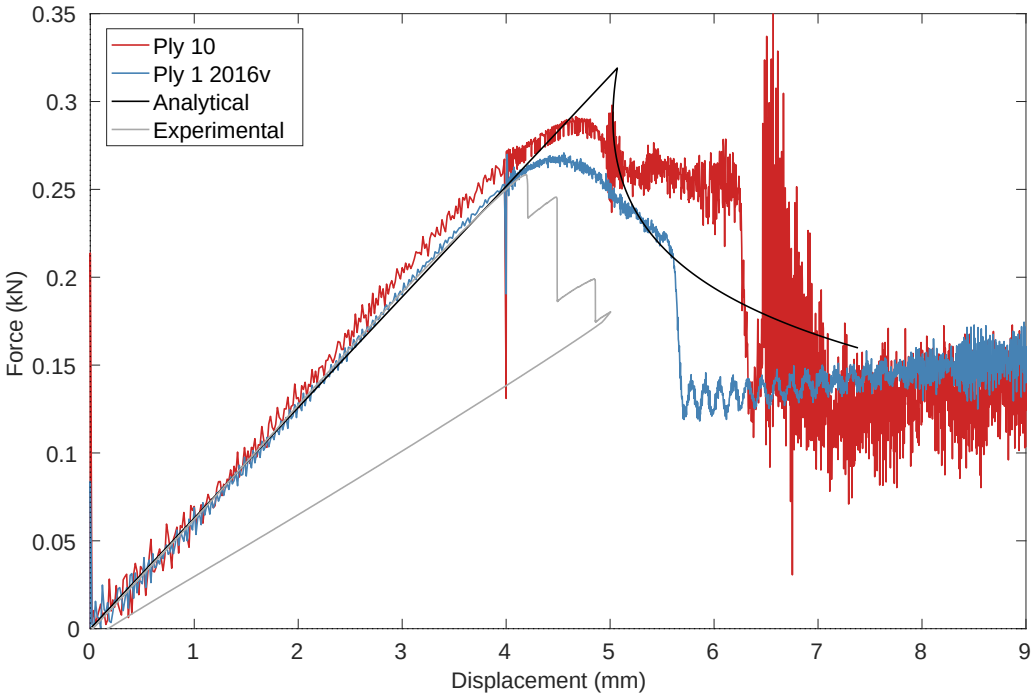

Figure 7.12: MMB results for the material CC with mixed-mode ratio 50% with an element size of 1.4 mm.

7.1.3 Low Velocity Impact test

In this section the numerical results for the Low Velocity Impact tests of the unidirectional carbon-reinforced composite (CC) are presented and discussed. For laminates L01 and L02, the LVI test is performed with impacts at different energetic configurations:

- IC1: Energy = 30J: Impactor mass $I_M = 3$ kg at a speed of $V_I = 4.47$ m/s.
- IC2: Energy = 20J: Impactor mass $I_M = 3$ kg at a speed of $V_I = 3.65$ m/s.

The force-time and the energy-time curves of the LVI test over the pure laminate L01 with the impact configuration IC1 are shown in Figures 7.13(a) and 7.13(b).

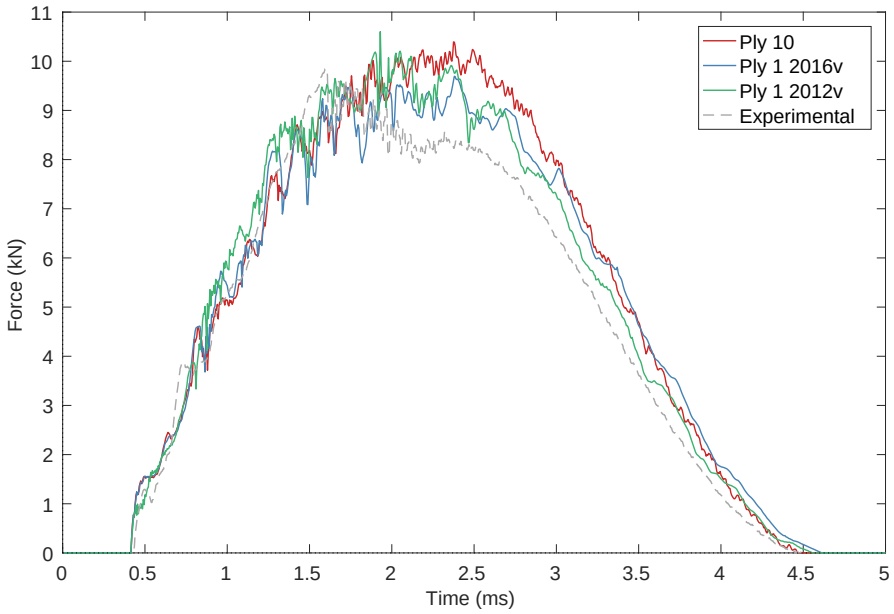

(a) Force-time

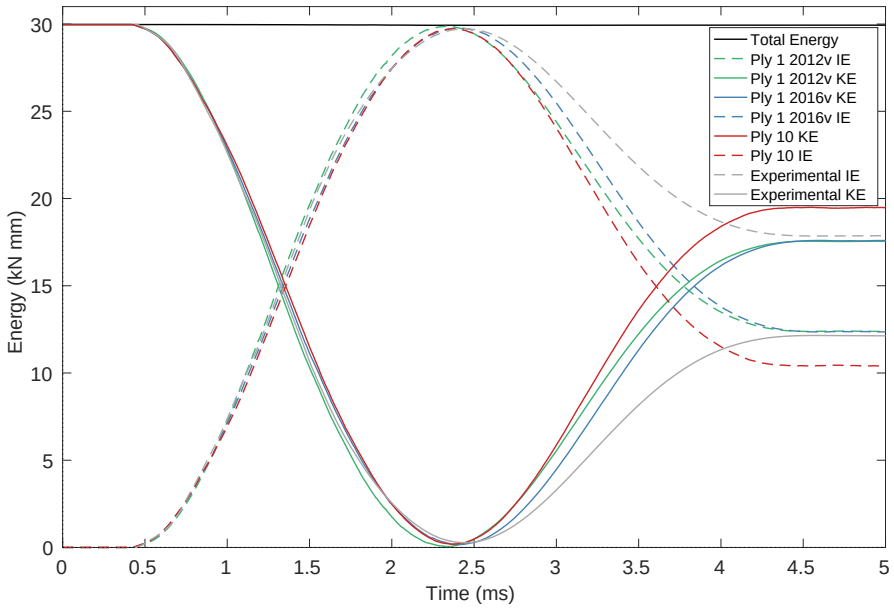

(b) Energy-time

Figure 7.13: Results for the LVI test on laminate L01 with the configuration IC1.

The force-time and the energy-time curves of the LVI test over the pure laminate L01 with the impact configuration IC2 are shown in Figures 7.14(a) and 7.14(b).

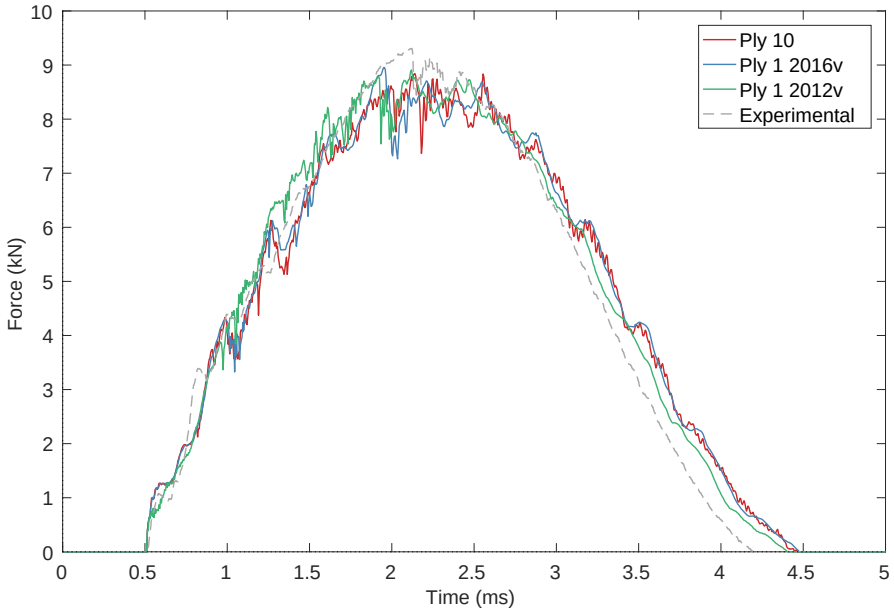

(a) Force-time

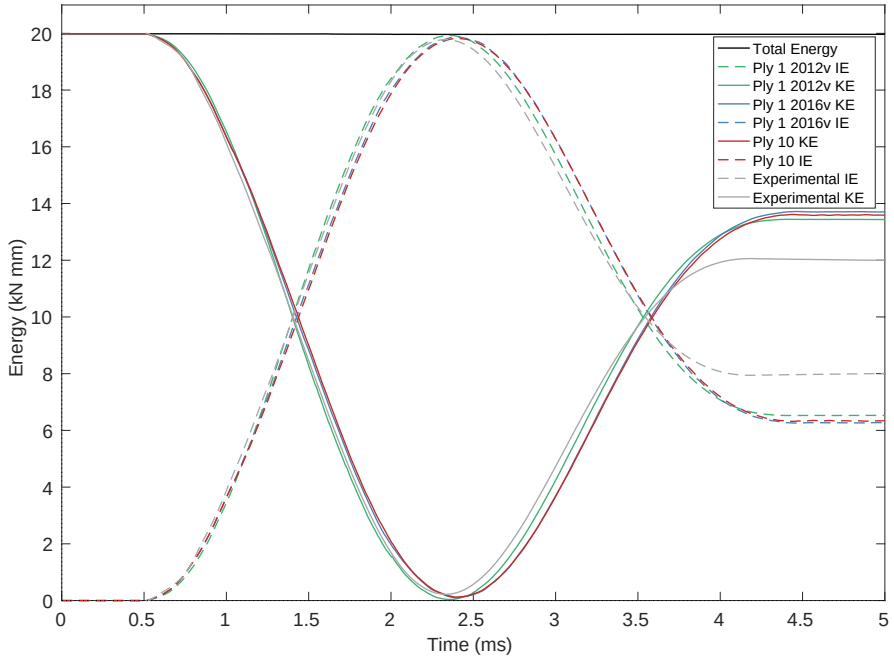

(b) Energy-time

Figure 7.14: Results for the LVI test on laminate L01 with the configuration IC2.

The force-time and the energy-time curves of the LVI test over the pure laminate L02 with the impact configuration IC1 are shown in Figures 7.15(a) and 7.15(b).

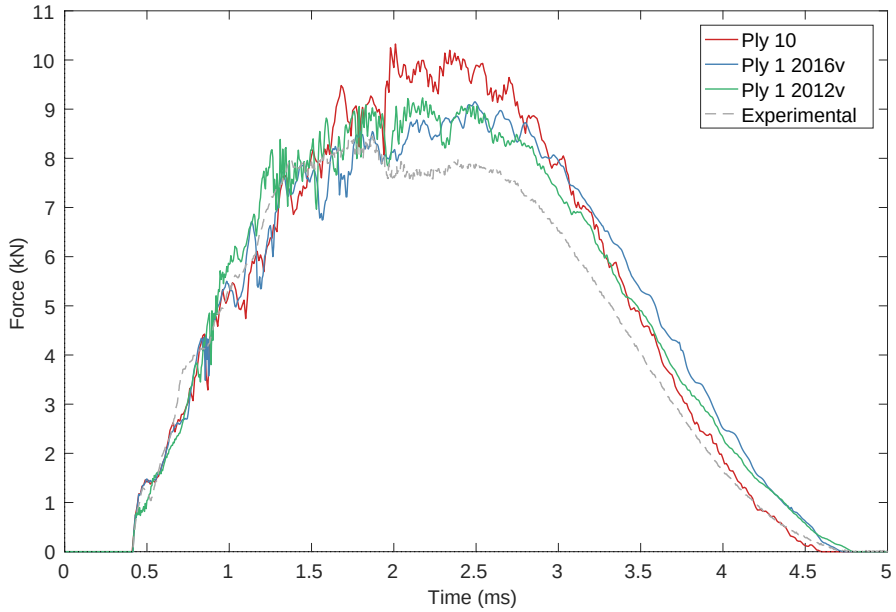

(a) Force-time

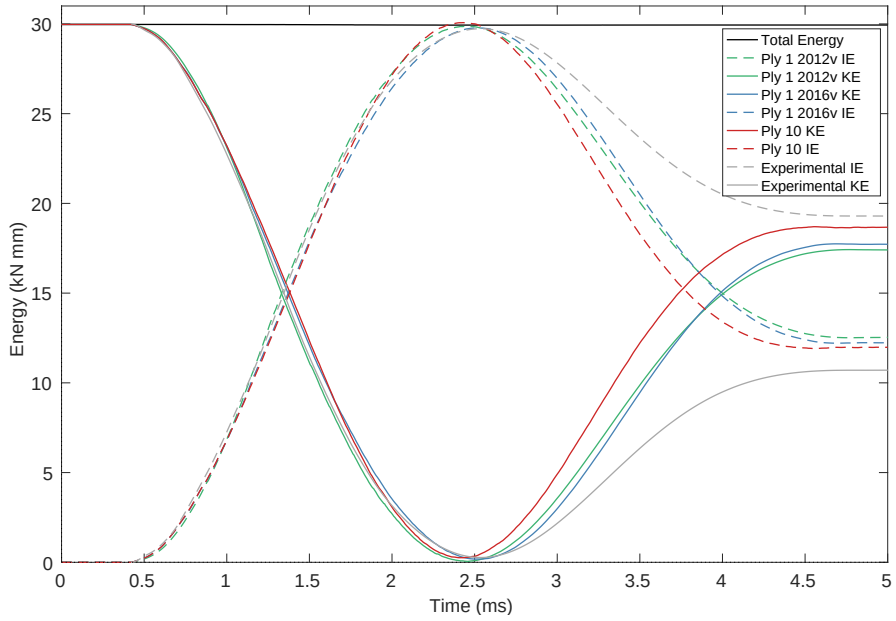

(b) Energy-time

Figure 7.15: Results for the LVI test on laminate L02 with the configuration IC1.

The force-time and the energy-time curves of the LVI test over the pure laminate L02 with the impact configuration IC2 are shown in Figures 7.16(a) and 7.16(b).

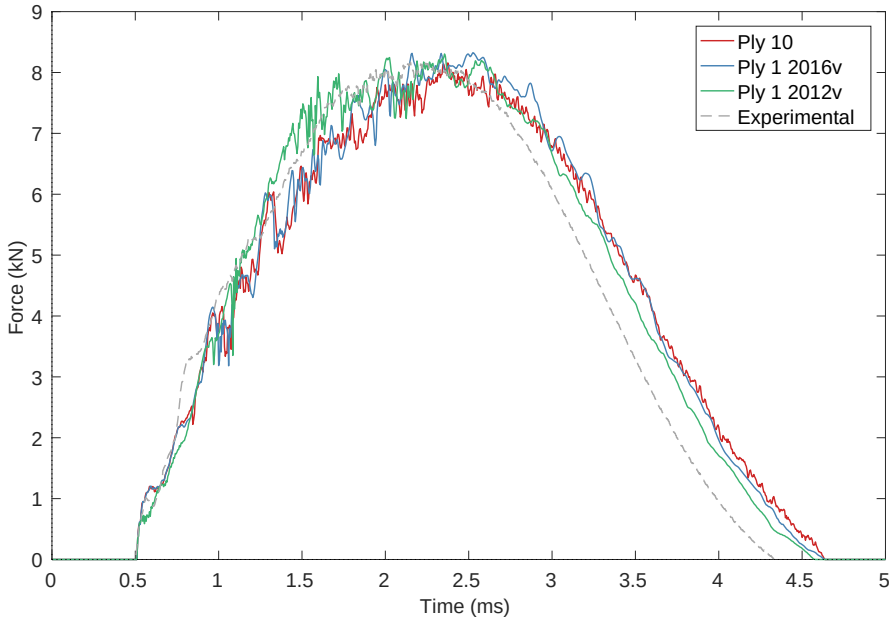

(a) Force-time

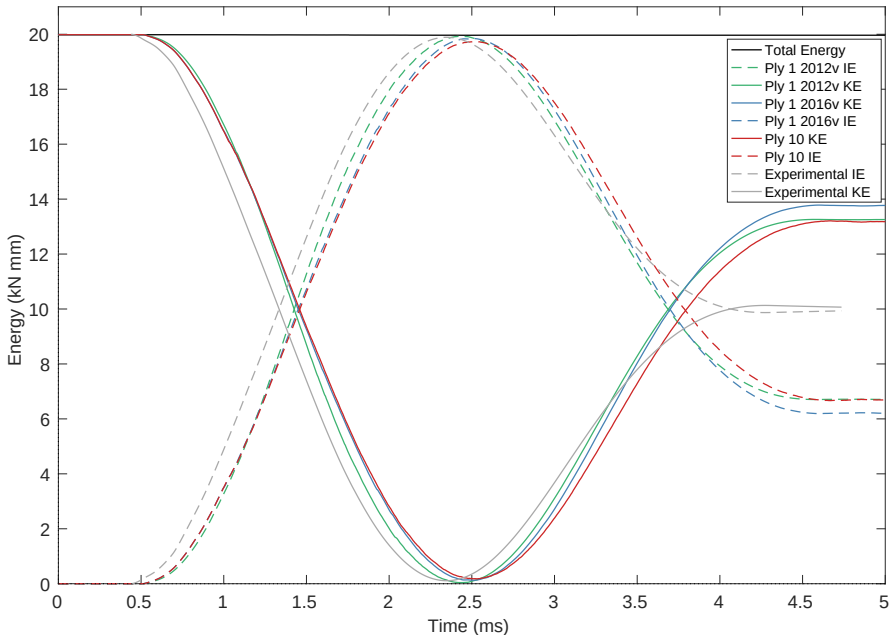

(b) Energy-time

Figure 7.16: Results for the LVI test on laminate L02 with the configuration IC2.

The first part of the force-time curve corresponds to the collision of the impactor with the specimen. Once the test begins, the kinetic energy that the impactor collides with is absorbed by the specimen. When the maximum value of force is reached all the kinetic energy has been transformed into internal energy. In the second part, the impactor rebounds. Therefore, the force exerted by the impactor on the specimen decreases and the internal energy is transformed back into the kinetic energy that bounces back the impactor.

The results presesented for Low Velocity Impact tests for each laminate with different configurations IC1 and IC2 show a good correlation between the experimental and numerical solutions. However, it can be observed how after the rebound, the numerical models are over estimated in force, as it can be seen in the energy-time curves, since the numerical specimen absorbs less amount of energy than the experimental one. Because of this, the impactor is bounced back with a greater amount of kinetic energy than in the experimental one. On the contrary to delamination tests, on LVI tests there are no significant differences between both ply model types and versions.

7.2 Material TC

7.2.1 One element tests

In this section, the results for the numerical simulations over one element models for each load case presented in Figure 6.3 are shown. For this, the stress-strain relation and the dissipated energy per area for element sizes of 5 mm and 1.4mm are presented for the ply models type 7 and 10. Once the behaviour of each damage mechanism of the model presented in Chapter 3 is validated, the ply properties use to define both ply models will be used in the posterior models for the fabric-reinforced composite material (TC).

In Figure 7.17 can be observed the comparisson of the stress-strain relation between the ply model type 7, model already implemented in Pam-Crash libraries, and ply model type 10, model implemented as a user-subroutine in this master thesis. Tensile and compressive loads correspond to red and blue lines, respectively, in the longitudinal and transverse direction. On the other hand, the dashed line corresponds to the ply model type 7, while the continuous line represents the results for the ply model type 10 (user-

subroutine). The stress-strain responses match with the expected damage mechanisms defined in Chapter 3 and ultimate strengths obtained in the experimental tests.
Furthermore, in Figure 7.18 the dissipated energy per area is represented. It can be seen how for both ply model types the obtained energy is the same, corresponding to the fracture toughness in each direction for each damage mechanism: $\mathcal{G}_{1T} = 0.045$ kN/mm, $\mathcal{G}_{1C} = 0.017$, kN/mm, which can be observed in Figure 7.18 (a), red and blue line, respectively. $\mathcal{G}_{2T} = 0.045$ kN/mm, $\mathcal{G}_{2C} = 0.017$ kN/mm, presented in Figure 7.18 (b), red and blue line, respectively.

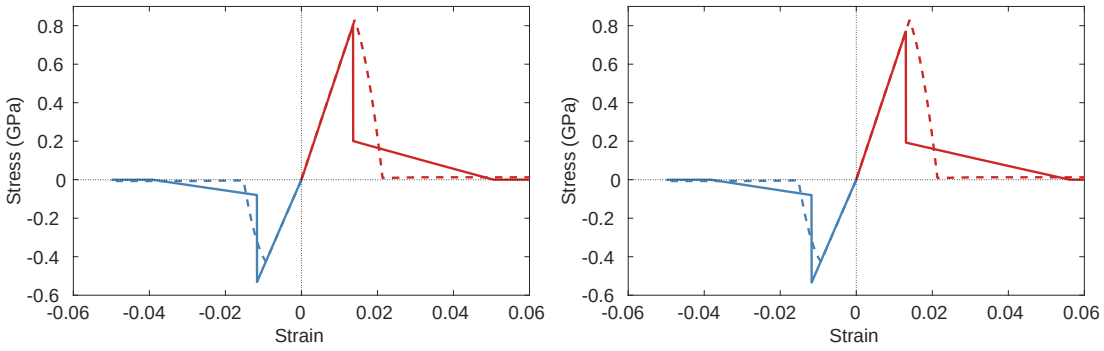

(a) Longitudinal direction (b) Transverse direction

Figure 7.17: Stress-strain curve for one element test for the material TC with an element size of 5 mm.

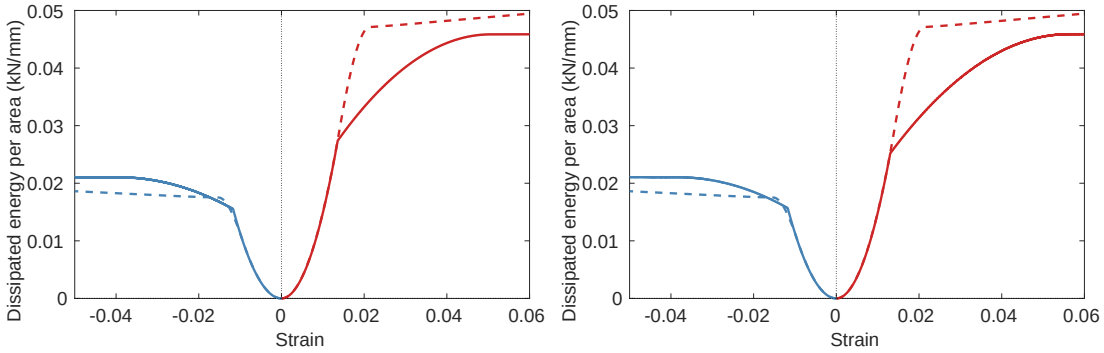

(a) Longitudinal direction (b) Transverse direction

Figure 7.18: Dissipated energy per area for one element test for the material TC with an element size of 5 mm.

The shear response is represented in Figure 7.19. For ply model type 7 a damage mechanism is considered in the shear direction, as can be observed in 7.19, while ply model type 10 does not show a damage mechanism in the shear direction but an isotropic hardening plastic deformation.

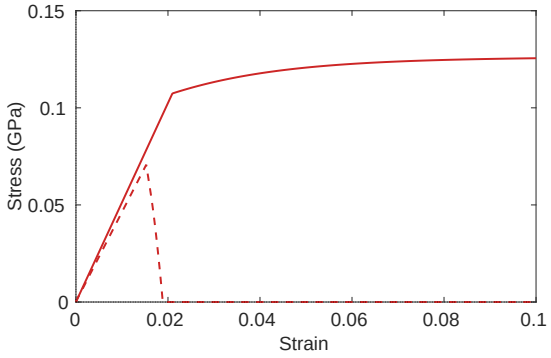

Figure 7.19: Stress-strain curve for a shear loaded element for the material TC with an element size of 5 mm.

As it has been explained in the previous chapter, the constitutive equations are also validated for an element size of 1.4 mm (Figures 7.20, 7.21 and 7.22).

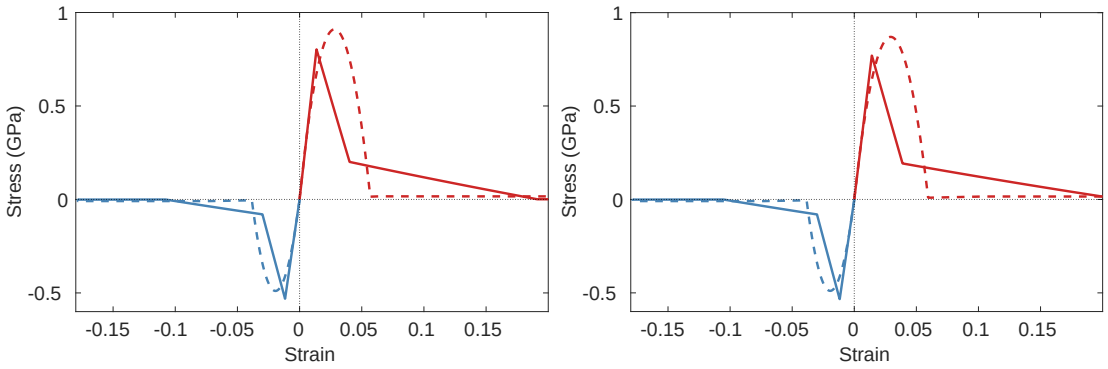

(a) Longitudinal direction (b) Transverse direction

Figure 7.20: Stress-strain curve for one element test for the material TC with an element size of 1.4 mm.

Comparing the warp, weft and shear responses for each element sizes, it can be observed that for each damage mechanism, the ultimate strength and dissipated energy per area are

equal for both element sizes for ply model type 10, demonstrating the mesh independency of the model implemented in this master thesis. While for ply model type 7, using the tools developed in the SUPERCALCULUS project, the dissipated energy per area is equal for both sizes of the element regardless the value of the ultimate strength or the shape of the constitutitve law.

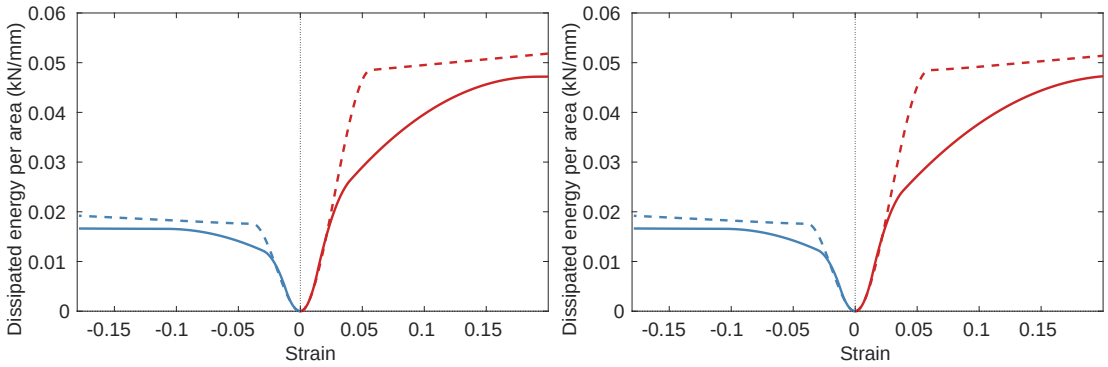

(a) Longitudinal direction (b) Transverse direction

Figure 7.21: Dissipated energy per area for one element test for the material TC with an element size of 1.4 mm.

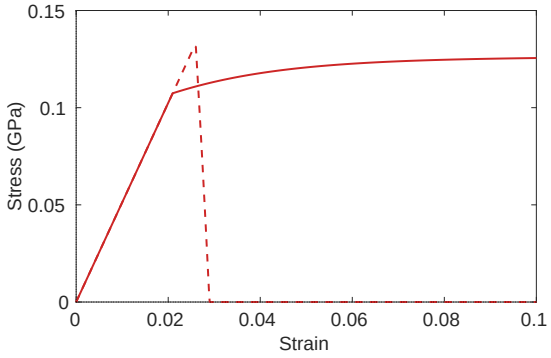

Figure 7.22: Stress-strain curve for a shear loaded element for the material TC with an element size of 1.4 mm.

7.2.2 Delamination

In this section, the results for the delamination tests of the fabric-reinforced composite (TC) are presented. In the first place, the numerical results for the pure modes I and II,

DCB and C-ELS, respectively, are shown. Once the properties of the interface have been adjusted for these modes, a mixed mode of delamination (MMB) is tested.
For this, the force-displacement curves for element sizes of 5 mm for the ply models type 7 and 10 are presented. For this material, the mesh influence in the material 303, which is the material used to define the mechanical properties used in the two tied interfaces, is not going to be studied due to its redundancy. Besides, the results obtained in the SUPERCALCULUS project using the ply model type 7 with the 2012 version of PAM-CRASH are presented in order to observe the differences between versions and how they have been overcome.

7.2.2.1 Mode I: DCB Tests

Numerical simulations of DCB tests, previously defined in Section 6.3, for the material TC an element size of 5 mm. are performed. The properties of the ply are the ones used in the one element tests, while the interlaminar properties are chosen according to the Table 5.4 and the reduced value of the interfacial strength $\tau_3^0 = 6.6$ MPa obtained in Chapter 6.

In Figure 7.23 the results obtained in the simulations for an element size of 5 mm are shown. It can be observed how numerical results lose precision in the peak where the delamination should be onset, due to the strength reduction for the delamination onset in the numerical model. After the delamination onset, numerical results for the propagation of the crack shows a good correlation level with the experimental and analytical results.

Regarding the differences between versions, the loss of precision is more pronounced in the 2016 version. However, this problem has been tried to be surpassed using the parameter IDEABEN equal to 4 instead of 0, as it has been explained in Section 6.3. Unlike for the CC material, the relation of stiffness between the principal directions, causes that the application of the different values for the IDEABEN parameter in the TC material does not lead to any notorious difference in the numerical results, independently of the ply model used. Therefore, on the force-displacement curve, it can be observed a higher difference between 2016 and 2012 version in the loss in the delamination onset.

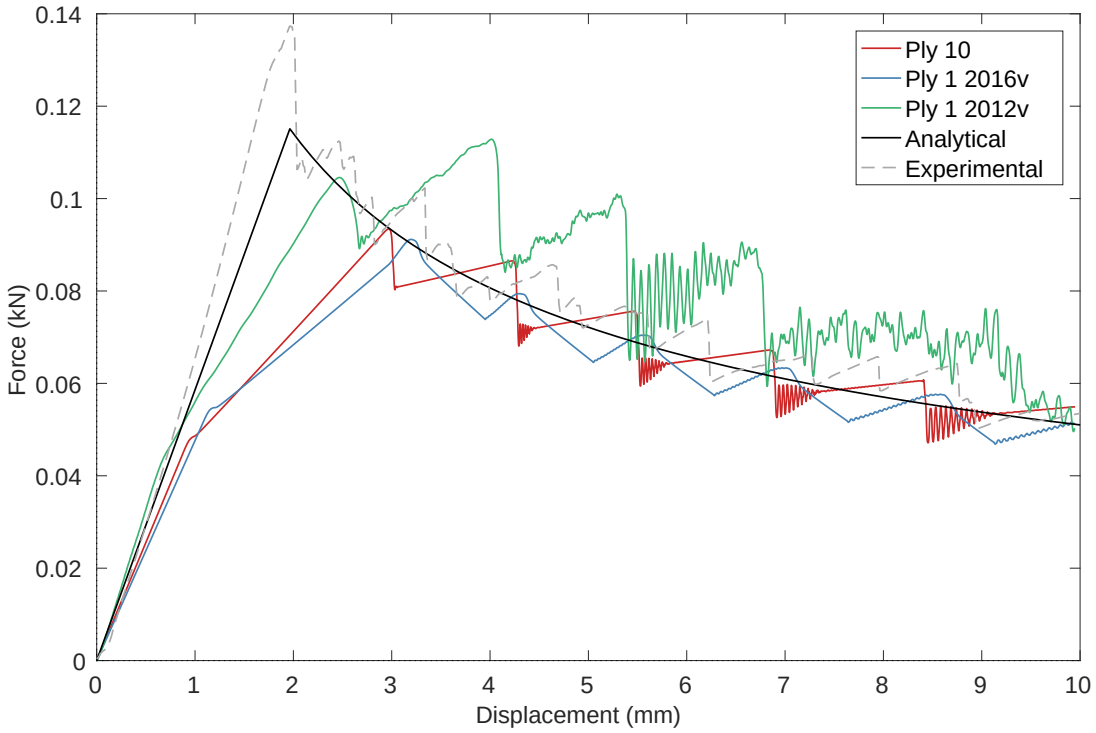

Figure 7.23: DCB results for the material TC with an element size of 5 mm.

7.2.2.2 Mode II: C-ELS Tests

Numerical simulations of C-ELS tests, previously defined in Section 6.3, for the material TC an element size of 5 mm. are performed. The properties of the ply are the ones used in the one element tests, while the interlaminar properties are chosen according to the Table 5.4 and the reduced value of the interfacial strength $\tau_{sh}^0 = 12$ MPa presented in Chapter 6.

In Figure 7.25 are shown the numerical results obtained for a value of the interfacial strength $\tau_{sh}^0 = 12$ MPa. It can be observed that for this value of τ_{sh}^0 the force-displacement relation does not capture the slope before the beginning of delamination nor the progression after it. Therefore, in order to obtain a better response for this test, the value of τ_{sh}^0 is adjusted manually. A value of $\tau_{sh}^0 = 30$ MPa is found to provide a better level of correlation, as it is shown in Figure 7.24. On the contrary to what happened in DCB tests, numerical results of C-ELS test for TC material capture the peak where the delamination should be onset. After the beginning of delamination the progression still matches with the experimental and analytical results. However, for the ply model type 7, the ply breaks

at 40 mm of displacement before the end of the test.

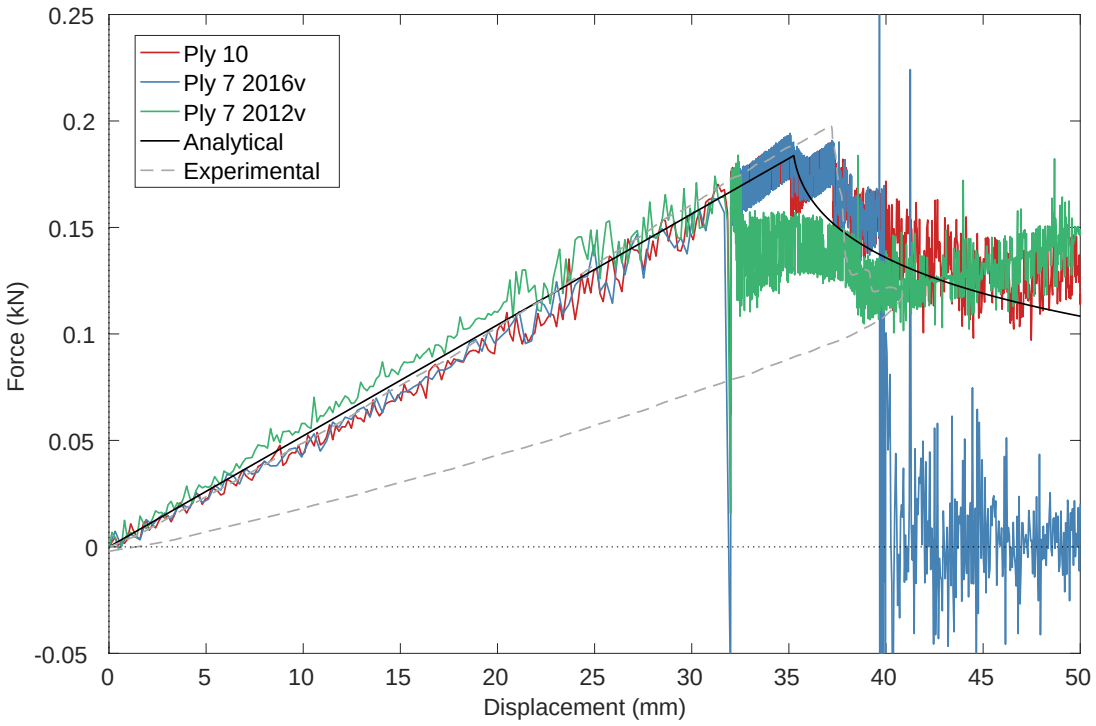

Figure 7.24: C-ELS results for the material TC with an element size of 5 mm $\tau_{sh}^{0} = 30$ MPa.

Regarding the differences between versions, in this case, using IDEABEN equal to 4 and the 2016 version of Pam-Crash it is not enough to improve the numerical results. But, when the value of the interfacial strength for mode II is adjusted manually, the force-displacement response is highly improved. As it can be observed in Figure 7.24, the numerical result for ply model type 7 using the 2012 version of Pam-Crash lose precision in the peak where delamination begins.

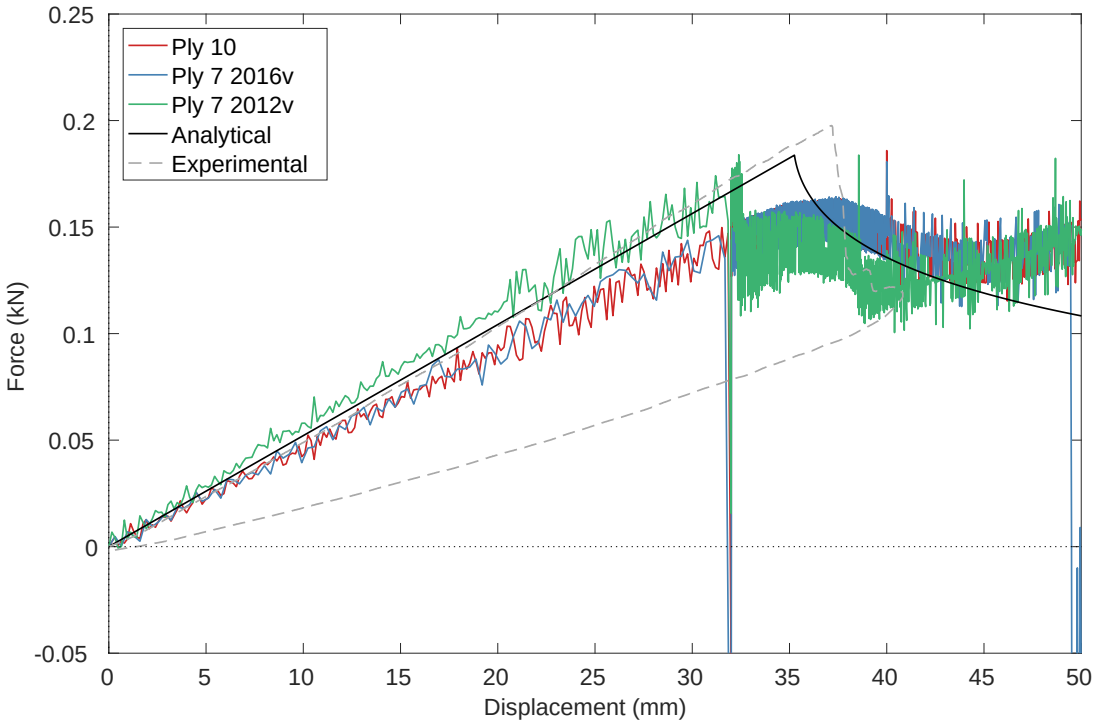

Figure 7.25: C-ELS results for the material TC with an element size of 5 mm $\tau_{sh}^{0} = 12$ MPa.

7.2.2.3 Mixed Mode: MMB Tests

Numerical simulations of MMB tests with a mixed mode of 50%, previously defined in Section 6.3, for the material TC an element size of 5 mm. are performed. The properties of the ply are the ones used in the one element tests, while the interlaminar properties are chosen according to the values used in the DCB and C-ELS tests.

Mixed mode of delamination gives a worse description on the force-displacement curve. As can be observed in Figure 7.26 the response obtained for both ply models using 2016 version is overestimated compared to the one obtained with 2012 version. Although, using the previous value of $\tau_{sh}^{0} = 12$ MPa, the one obtained in Chapter 6, a better level of correlation is found (Figure 7.27). The accuracy of the slope and the peak before delamination as well as the progression after it is highly improved.

For mixed modes, a value of $\tau_{sh}^0 = 12$ MPa captures better the damage in delamination, while for pure modes I and II there is a loss of precision in both the slope and the progression of the damage. Because of this, $\tau_{sh}^0 = 30$ MPa is chosen as the reduced interfacial strength. In any case, this reduced values of the interfacial strength are only used in delamination tests, since for LVI tests the original values obtained from the experimental tests are used.

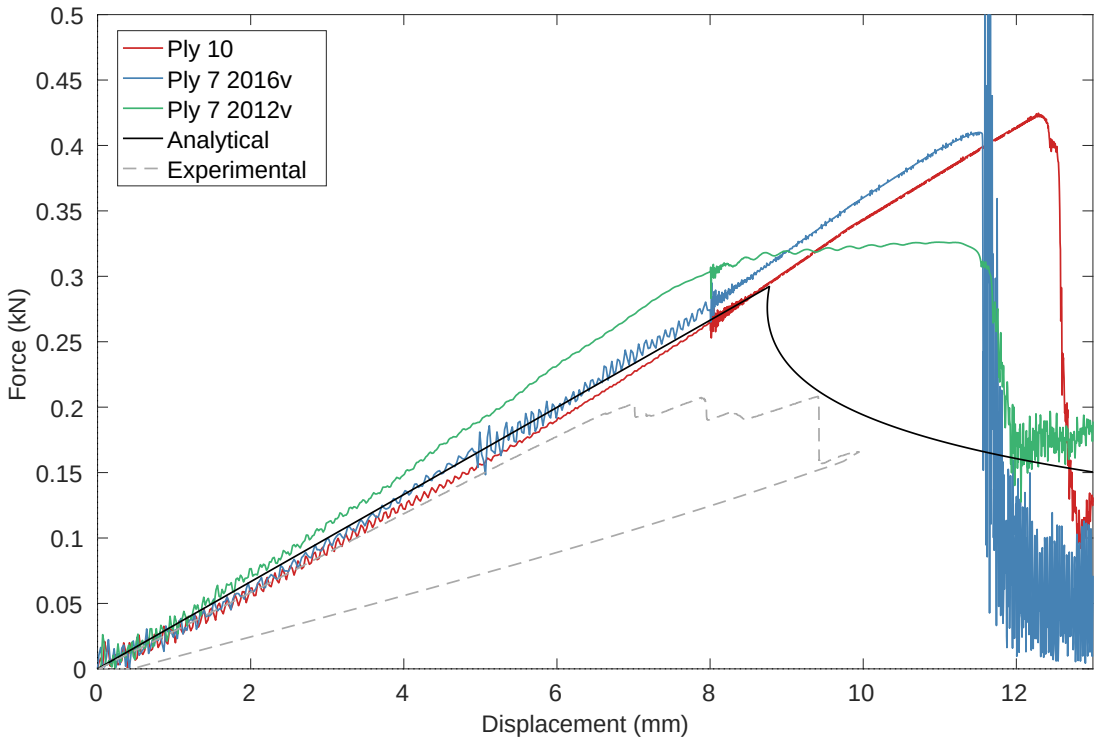

Figure 7.26: MMB results for the material TC with mixed-mode ratio 50% with an element size of 5 mm for $\tau_{sh}^0 = 30$ MPa.

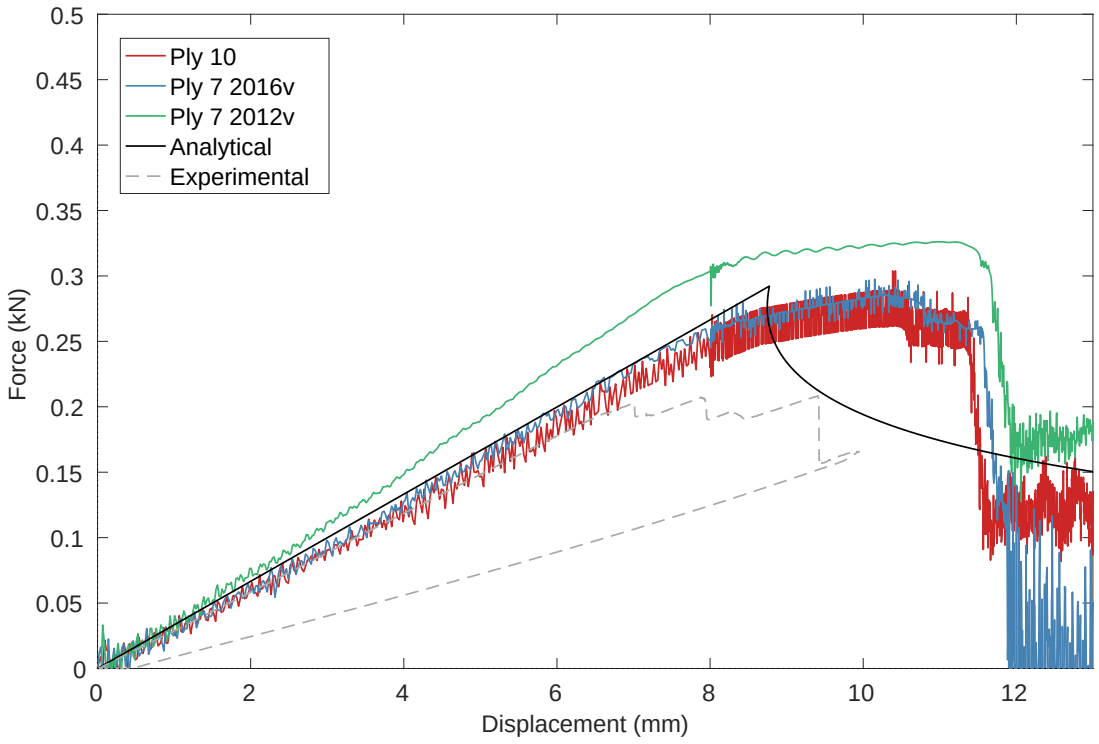

Figure 7.27: MMB results for the material TC with mixed-mode ratio 50% with an element size of 5 mm $\tau_{sh}^{0} = 12$ MPa.

7.2.3 Low Velocity Impact test

In this section the numerical results for the Low Velocity Impact tests of the fabric reinforced composite (TC) are presented and discussed. For laminate L03, the LVI test is performed with impacts at different energetic configurations:

- IC1: Energy = 30J: Impactor mass $I_M = 3$ kg at a speed of $V_I = 4.47$ m/s.
- IC2: Energy = 40J: Impactor mass $I_M = 5$ kg at a speed of $V_I = 4.00$ m/s.

The force-time and the energy-time curves of the LVI test over the pure laminate L03 with the impact configuration IC1 are shown in Figures 7.28(a) and 7.28(b).

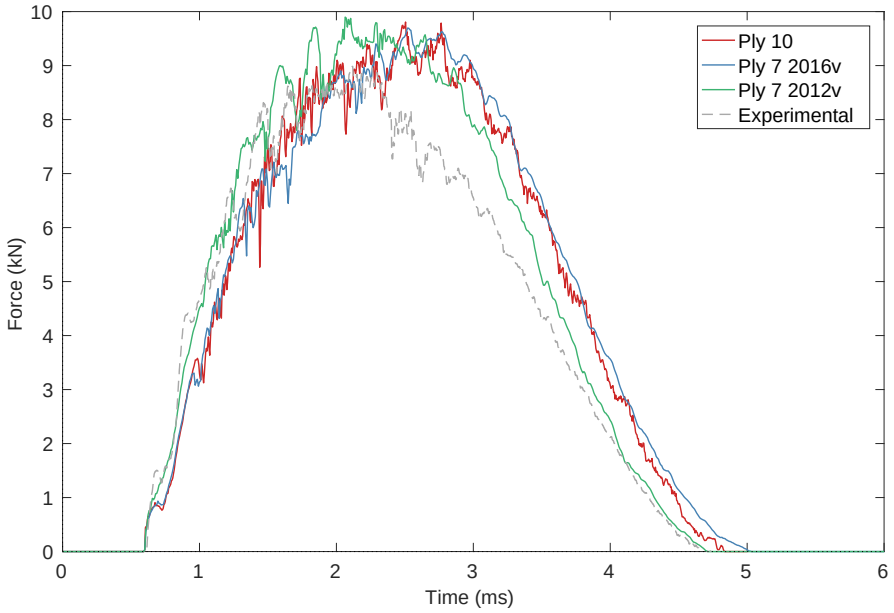

(a) Force-time

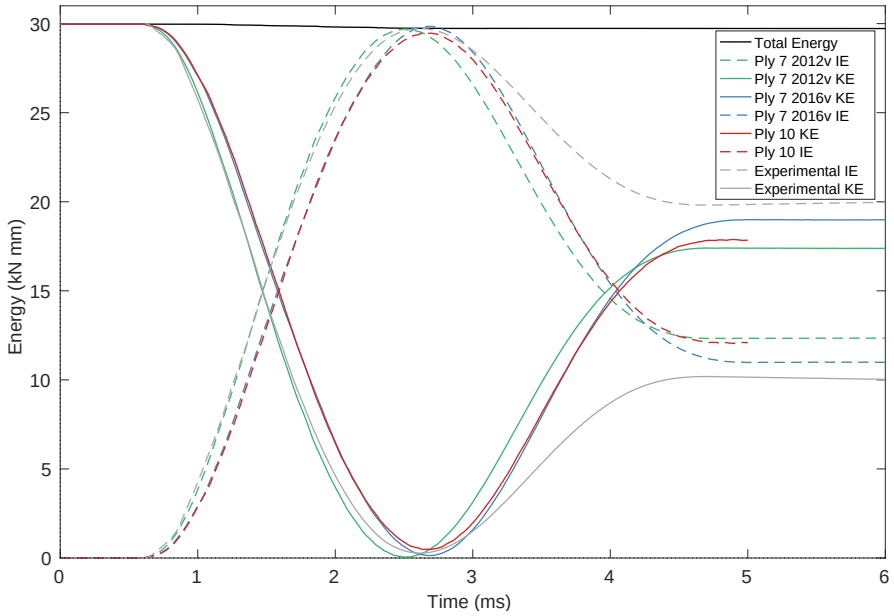

(b) Energy-time

Figure 7.28: Results for the LVI test on laminate L03 with the configuration IC1

.

The force-time and the energy-time curves of the LVI test over the pure laminate L03 with the impact configuration IC2 are shown in Figures 7.29(a) and 7.29(b).

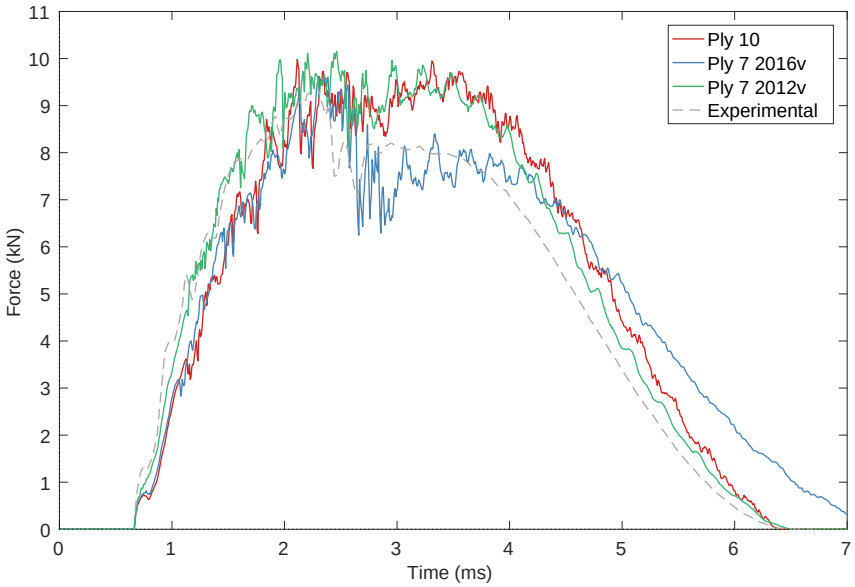

(a) Force-time

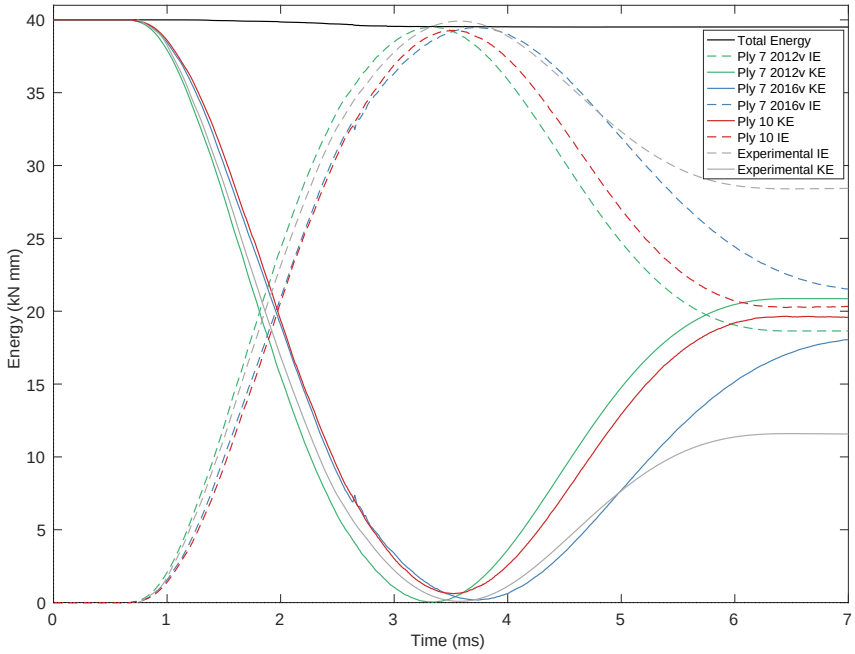

(b) Energy-time

Figure 7.29: Results for the LVI test on laminate L03 with the configuration IC2

.

The first part of the force-time curve corresponds to the collision of the impactor with the specimen. Once the test begins, the kinetic energy that the impactor collides with is absorbed by the specimen, when the maximum value of force is reached all the kinetic energy has been transformed into internal energy. In the second part, the impactor rebound. Therefore, the force exerted by the impactor on the specimen decreases and the internal energy is transformed back into the kinetic energy that bounces back the impactor.

The results presesented for Low Velocity Impact tests for laminate L03 conformed with material TC with different configurations IC1 and IC2 show a worse correlation between the experimental and numerical solutions. The numerical models are over estimated in terms of force after the rebound than for CC material. When the impact energy is risen, the differences between the numerical and experimental results are also increased, as well as the differences between ply model types and versions. In Figure 7.29 these differences can be observed, concluding that a better correlation is achieved with ply model type 1 2012 version and ply model type 10.

Chapter 8

Conclusions and future research lines

A major challenge relating to automotive composite design is the availability of simulation tools and a general lack of composite material characterization. In this way, the proper characterization and definition of the constitutive behaviour of composite materials are required in order to simulate complete car models in different crash conditions.

The aim of this thesis was to develop, implement and validate a constitutive model for the simulation of carbon fibre-reinforced polymers at a mesoscale level under impact loading in Pam-Crash Finite Element (FE) code using Fortran. For this, the model developed by Martín-Santos et al. in 2013 has been taken as a reference, in which a cohesive law-based formulation to describe the degradation of the mechanical properties for the implemented damage mechanisms, and an isotropic hardening plasticity for the in-plane shear behaviour, are used. In addition, the Crack Band Methodology has been implemented in order to reduce the mesh influence in the results.

The Continuum Damage Model presented in this work has been validated by comparing the results of FE simulations with experimental and analytical data from: delamination tests, used to characterize the interfase properties, and Low Velocity Impact tests, used to analyse the performance of large specimens causing a combined state of damages in the material. Moreover, the constitutive laws were validated by the performance of tests over one element for different loading conditions. A study of mesh size requirements has been made, in order to ensure a balance between the precision of the solution and the computational cost, resulting in element sizes of 5 mm and 1.4 mm, which were the ones used in the numerical models.

The model is able to reproduce the behaviour of a wide range of materials. In this work two types of materials have been used for the simulation of the different tests: Unidirectional cabron-reinforced composite (CC) and fabric carbon-reinforced composite (TC). Experimental results and material data were provided in the SUPERCALCULUS project.

Numerical simulations were performed using the ply model type 10, corresponding to the user-subroutine implemented in this master thesis. In addition, in order to check the validity of our model, the numerical tests were also performed using the ply models already implemented in PAM-CRASH libraries, corresponding to ply model type 1 for CC material and ply model type 7 for TC material. The numerical models developed in SUPERCALCULUS were adapted to the 2016 version of PAM-CRASH. Therefore, the results obtained in this project have been compared with the ones obtained in the SUPERCALCULUS project.

The mesh independecy of the model was desmonstrated through one-element test simulations, since the values of ultimate strengths and dissipated energies per area obtained for each damage mechanism are identical for different element sizes using the same material definition. Whereas, for ply models type 1 and 7, in order to achieve an equivalent toughness level, two different material cards must be define for two different element sizes. On the other hand, the numerical simulations of delamination and low velocity impact tests produced a good correlation between the different ply models and versions, with their corresponding adjustments due to the change of version of PAM-CRASH.

8.1 Future research lines

In this section, the future research lines opened by this work are presented below.

- On PAM-CRASH ply models, the sitffness properties of the plies are degraded until a damaged shell element is eliminated from the computation when the damage reaches a predefined saturation value. In user-subroutines models, the control of the elimination of elements is not possible unless it is implemented. Thus, a control of element elimination will be implemented in the model presented in this thesis, in order to be able to simulate tests in which this performance is critical.

- Development and implementation of a new inter-laminar formulation to improve delamination without the need of using the engineering solution, due to its limina-tions.

- Application of the model in real components of the automobile. Since IDIADA is involved in several projects regarding FRPs, the developed material model will be tested in simulations for ongoing projects.

- Upgrade the model to n-linear cohesive laws to define the damage evolution in a ply.

Bibliography

[1] Martín-Santos, E., Maimí, P., Gonzalez, E. V., and Cruz, P.(2014). A continuum constitutive model for the simulation of fabric-reinforced composites. *Compos Sci Technol*, 111,122-129.

[2] Martín-Santos, E. (2011). *Informe inicial de estudio de posibilidades de PAMCRASH.* (Documento inédito). AMADE Análisis y Materiales Avanzados para el Diseño Estructural. Escola Politècnica Superior. Universitat de Girona.

[3] Martin-Santos, E. (2013) *Informe Intralaminar.* (Documento inédito). AMADE Análisis y Materiales Avanzados para el Diseño Estructural. Escola Politècnica Superior. Universitat de Girona.

[4] Cox, B. N., and Flanagan, G. (1997). *Handbook of analytical methods for textile composites.* NASA contractor report 4750.

[5] Masuelli, A. (2013) *Introduction of Fibre-Reinforced Polymers − Polymers and Composites: Concepts, Properties and Processes.* InTech.

[6] Andersson, M., and Liedberg, P. (2014). *Crash behavior of composite structures. A CAE benchmarking study.* (Master Thesis). Department of Applied Mechanics. Chalmers University of Technology.

[7] Ladèveze, P., and LeDantec, E.(1992) Damage modelling of the elementary ply for laminated composites. *Compos Sci Technol*, 43,257-67.

[8] Ladèveze, P.(1992) A damage computational method for composite structures. *Comput Struc*, 44,79-87.

[9] Hochard, C., Aubourg, P., and Charles, J.(2001). Modelling of the mechanical behaviour of woven-fabric CFRP laminates up to failure. *Compos Sci Technol*, 61,221-30.

[10] Hochard, C., and Thollon,Y.(2010). A generalized damage model for woven ply laminates under static and fatigue loading conditions. *Int J Fatigue*, 32,158-65.

[11] Johnson, A. F., Pickett, A. K, and Rozycki,P.(2001). Computational methods for predicting impact damage in composite structures. *Compos Sci Technol*, 61,2183-92.

[12] Fouinneteau, M.(2006). *Damage and failure modelling of carbon and glass 2D braided composites*. (PhD thesis). Cranfield University. School of Applied Sciences.

[13] Matzenmiller, A., Lubliner, J., and Taylor, R. L.(1995). A constitutive model for anisotropic damage in fiber-composites. *Mech Mater*, 20,125-52.

[14] Böhm, R., Gude, M., and Hufenbach, W.(2011). A phenomenologically based damage model for 2D and 3D-textile composites with non-crimp reinforcement. *Mater Des*, 32,2532-44.

[15] Iannucci, L., Dechaene, R., Willows, M., and Degrieck, J.(2001). A failure model for the analysis of thin woven glass composite structures under impact loadings. *Comput Struct*, 79,785-99.

[16] Bažant, Z., and Oh, B. H.(1983). Crack band theory for fracture of concrete. *Matér et Constr*, 16,155-77.

[17] Iannucci, L., and Willows, M. L.(2007). An energy based damage mechanics approach to modelling impact onto woven composite materials - Part II. Experimental and numerical results. *Compos Part A: Appl Sci Manuf*, 38,540-54.

[18] Bao, G., Suo, Z. (1992). Remarks on crack-briding concepts. *Appl Mech Rev*, 45,355-66.

[19] Foote, R. M. L., Mai, Y-W., and Cotterell, B. (1986). *J Mech Phys Solids*, 34,593-607.

[20] Jacobsen, T. K., Sørensen, B. F. (2001). Mode I intra-laminar crack growth in composites-modelling of R-curves from measured bridging laws. *Compos Part A Appl Sci Manuf*, 32,1-11.

[21] Dopker, B., Murphy, D. P., Ilecwicz, L. B., and Walker, T. (1994). Damage tolerance analysis of composite transport fuselage structure. *35th AIAA/ASME/ASCE/AHS structures, structural dynamics and materials conferences.*

[22] Miamí, P., Camanho, P. P., Mayugo, J. A., and Dávila, C. G.(2007). A continuum damage model for composte laminates: Part I - Constitutive model. *Mech Mater*, 39,897-908.

[23] Miamí, P., Camanho, P. P., Mayugo, J. A., and Dávila, C. G.(2007). A continuum damage model for composte laminates: Part II - Computational implementation and validation. *Mech Mater*, 39,909-19.

[24] Dávila, C. G., Rose, C. A., and Camanho, P. P. (2009). A procedure for superposing linear cohesive laws to represent multiple damage mechanisms in the fracture of composites. *Int J Fract*, 158,211-23.

[25] Welsh, J. S., Mayers, J. S., Key, C. T., and McLaughlin, R. N. (2004). Comparison of MCT failure prediction techniques and experimental verification for biaxially loaded glass frabric-reinforced composite laminates. *J Compos Mater*, 38,2165-81.

[26] Adams, D. F., Carlsson, L. A., Pipes, R. B. (2003). *Experimental Characterization of Advanced Composite Materials*. CRC Press.

[27] Camanho, P., and Dávila, C. (2002). Mixed-mode decohesion finite elements for the simulation of delamination in composte materials. *NASA REPORT: NASA/TM-2002-211737*,

[28] Turon, A., Dávila, C. G., Camanho, P. P., and Costa, J.(2006). An engineering solution for mesh size effect in the simulation of delamination using cohesive zone models. *Engineering Fracture Mechanics*, 74,1665-82.

[29] Turon, A., Costa, J., Camanho, P. P., and Miamí, P.(2008). Analytical and numerical investigation of the length of the cohesive zone in delaminated composte materials. *Computational Methods in Applied Sciences*, 10.

[30] Turon, A.(2006). *Simulation of delamination in composites under quasi-static and fatigue loading using cohesive zone models*. (PhD thesis). Universitat de Girona.

[31] Turon, A., Camanho, P. P., Costa, J., and Renart, J.(2010). Accurate simulation of delamination growth under mixed loading using cohesive elements: Definition of interlaminar strengths and elastic stiffness. *Composite Structures* 92,1857-64.

[32] Jiang, H. (2010). *Cohesive zone model for carbon nanotube adhesive simulation and frature/fatigue crack growth* (PhD Thesis). University of Akron.

[33] Stigh, U., and Svensson, D. (2010) On cohesive laws for delamination of composites. *14th European conference on composite materials.*

[34] Needleman, A. (2014). Some issues in cohesive surface modeling. *Procedia IUTAM*, 10,221-46.

[38] Pinho, S. T., Robinson, P., and Iannucci, L. (2006). Fracture toughness of the tensile and compressive fibre failure modes in laminated composites. *Composites Sci and Technol*, 66, 2069-79.

[36] Miamí, P., Trias, D., González, E. V., and Renart, J. (2012). Nominal strength of quasi-brittle open hole specimens. *Composites Sci and Technol*, 72, 1203-08.

[37] Miamí, P., González, E. V., Gascons, N., and Ripoll, L. L. (2013). Size effect law and critical distance theories to predict the nominal strength of quasibrittle structures. *Appl Mech Rev*, 65,1-16.

[38] Pinho, S. T., Robinson, P., and Iannucci, L. (2006). Fracture toughness of the tensile and compressive fibre failure modes in laminated composites. *Compos Sci Technol*, 66,2069-79.

[39] ESI. PAM-CRASH-Virtual Performance Solution 2016 Solver Reference Manual.